Chapter 17
Research on the Yb^{3+} Ion Activated Cubic Molybdates and Molybdato-Tungstates for Optical Transparent Ceramics

M. Guzik, M. Bieza, E. Tomaszewicz, Y. Guyot, and G. Boulon

Abstract As widely known, un-doped and rare earth-doped molybdates and tungstates are promising group which have attracted great attention in wide branches of optical material application not only as laser hosts but also as phosphors and scintillators. Most of laser host materials have been obtained as single crystals by Czochralski method. However, the materials in the form of transparent ceramics have comparable or even better important properties than single crystals.

Nowadays, a challenge is to obtain a high quality optical material based on new polycrystalline ceramics applied for laser sources, scintillators and phosphors and to improve manufacturing methods. Nevertheless, only few compositions of cubic transparent ceramics are actually well-developed, these include rare earth (RE^{3+})-doped garnets (Nd^{3+}/Yb^{3+}-doped $Y_3Al_5O_{12}/Lu_3Al_5O_{12}$, Ce^{3+} – doped $Y_3Al_5O_{12}$, fluorides (Yb^{3+}-doped CaF_2), RE^{3+}-doped sesquioxides (Nd^{3+}/Yb^{3+}-doped Lu_2O_3, Sc_2O_3, Y_2O_3) and also perovskite type BMT ($Ba(MgZrTa)O_3$) and un-doped spinel ($MgAl_2O_4$).

This is why our attention is focused on fabrication of new rare-earth doped molybdates or tungstates in the form of polycrystalline ceramics, unknown until now in the literature. The manufacture of ceramics takes less time, even only few days in contrast to 4–6 weeks to grow crystals by using the Czochralski method. In comparison with single crystals it is possible to receive samples highly activated by rare earth ions and of large size ceramics in much cheaper way without using

M. Guzik (✉) · M. Bieza
Faculty of Chemistry, University of Wrocław, Wrocław, Poland
e-mail: goguzik@poczta.fm

E. Tomaszewicz
Department of Inorganic and Analytical Chemistry, West Pomeranian University of Technology, Szczecin, Poland

Y. Guyot · G. Boulon
Univ Lyon, Université Claude Bernard Lyon1, CNRS, Institut Lumière Matière, Villeurbanne, France

B. Di Bartolo et al. (eds.), *Quantum Nano-Photonics*, NATO Science for Peace and Security Series B: Physics and Biophysics,
https://doi.org/10.1007/978-94-024-1544-5_17

expensive iridium or rhenium crucibles. Indeed, two conditions must be fulfilled to obtain transparent ceramics: the compounds should crystallize in the cubic system and the size of the crystallites must be in the order of tens of nanometers.

We present and discuss the structural (XRD and SEM analysis) and spectroscopic properties of three types of materials representing the family of Yb^{3+}-doped molybdates and molybdato-tungstates synthesized by the high-temperature solid-state reaction for future new optical ceramics crystallizing in the cubic system: $La_2Mo_2O_9$ /La_2MoWO_9 /Y_6MoO_{12}. Yb^{3+} rare earth ions has been selected since they can be substitute with trivalent La^{3+} and Y^{3+} cations and then can play the role of a structural probe and, in addition, can be used as laser ions in these materials.

17.1 Introduction

The rapid development of technology stimulates interest in substances that as a result of excitation can efficiently emit light-phosphor materials but also new high power efficient laser materials. Among inorganic matrices very well known, extensively studied and efficient as phosphors, scintillators and laser materials are tungstates and molybdates because of their thermal and chemical stability. In the literature, the most investigated groups are $CaWO_4$ and $MgWO_4$ as phosphors, as well as $ZnWO_4$, $CdWO_4$, and $PbWO_4$ as scintillators [1–8]. Additionally, Nd^{3+}-doped $CaWO_4$ was the first continuously operating crystal laser reported in 1961. Well known laser materials are $MRE(WO_4)_2$ (M = alkali metal, RE = Y, Gd, Lu) doped with optically active trivalent rare-earth ions such as Nd, Dy, Ho, Er, Tm, or Yb. Both Nd^{3+}- and Yb^{3+}-doped KGd $(WO_4)_2$ and KY $(WO_4)_2$ crystals became very important laser materials for near-infrared region [9–12]. Also, phosphors like Eu-doped $MgWO_4$, [13] Eu-doped $ZnWO_4$, [14] or Ce-doped MWO_4 (M = Ca, Sr, Ba) phosphors [15] have been recently published. Moreover, like for the tungstate family, un-doped and rare earth-doped $MMoO_4$ (M = Ca, Sr, Ba, Pb, and Cd) also form a wide class of materials used in different fields such as scintillators, phosphors, photoconductive and photocatalytic materials, as can be seen in these mentioned references as well as therein [16–24].

Our scientific program involves with trivalent rare earth ions doped $CdMoO_4$ scheelite-type cadmium molybdate. As an example, materials with the chemical formula of $Cd_{1-3x}Eu_{2x}\square_xMoO_4$ (cationic vacancy is denoted by $\square$) was investigated as a strong, pure, red-emitting phosphor for white light emitting diodes (WLEDs) by taking advantage of the Eu^{3+} spectroscopic probe ion to analyze in detail the structural properties as a continuation of our previous analysis on both, $Cd_{1-3x}Nd_{2x}\square_xMoO_4$ and $Cd_{1-3x}Yb_{2x}\square_xMoO_4$ characterized by very strong emission in the NIR region [25–27].

In last years increasing interest of development of the ceramic laser materials has been observed as the most important innovation of laser material fabrication technology. The polycrystalline ceramics possess many advantages in comparison to single-crystals; large size, a great number of varieties of shapes, better mechanical strength, higher content of doping activators, lower temperature of synthesis, less

time consuming, cheaper manufacturing process, and ability to engineer profiles and structures, which, moreover, do not require expensive equipment [28–31].

Indeed, two conditions must be fulfilled to obtain transparent ceramics: the compounds should crystallize in the cubic system and the size of the crystallites must be in the order of tens of nanometers. The above-mentioned advantages of the production of transparent ceramics are the reasons why a tendency to replace single crystals by transparent ceramics is observed. Surprisingly, today available rare earth (RE^{3+}) luminescent ions doped cubic optical transparent ceramics used as laser sources or phosphors for lighting are limited to a very small number.

Until now, only few transparent ceramics are known as optical materials with oxides (garnets, sesquioxides, spinels) and fluorides. Especially, we can mention the following references for laser materials:

- Nd^{3+}-doped $Y_3Al_5O_{12}$ garnets [32] In fact, Nd^{3+}:YAG ceramics has been fabricated and used to demonstrate an output power at 1.06 μm of 67 [33] and > 100 kW, [34] respectively.
- Yb^{3+}-doped $Y_3Al_5O_{12}$ ceramics [35, 36]
- Yb^{3+}-doped Y_2O_3 ceramics made by hot pressing of high submicron purity coprecipitated powder for high power solid-state lasers exploiting hosts with higher thermal conductivity than YAG [31]
- Nd^{3+}-doped Lu_2O_3 sesquioxide ceramics fabricated by Hot Isostatic Pressure (HIP) procedure [37]. Laser oscillation has been observed in hot pressed 10% Yb^{3+}-doped Lu_2O_3 ceramics [38]
- Nd^{3+}-doped Lu_2O_3 sesquioxide ceramics fabricated by the Spark Plasma Sintering (SPS) procedure [39, 40]
- Nd^{3+}, Yb^{3+}-co-doped SrF_2 laser ceramics [41]

Due to many advantages of rare earth-doped molybdate and tungstate compounds which fit several requests for optical materials, such as good mechanical strength, thermal property and chemical stability, our research was carried out toward new cubic ceramic optical materials different from those already known. The main objective is to succeed the challenge of synthesis of some rare earth ions (Ce^{3+}, Nd^{3+}, Eu^{3+}, Yb^{3+})-doped cubic tungstate and molybdate inorganic materials accompanied by structural and spectroscopic characterizations, within the expected goal of future innovative optical transparent ceramics.

The RE-doped $La_2Mo_2O_9$ molybdates crystallizing in monoclinic and cubic system were very little studied as the luminescent materials, while there are well-known as fast oxide-ion conductors and have been examined for catalytic applications [42, 43]. Only few articles reported optical properties of $La_2Mo_2O_9$ activated by the rare earth ions. However, the authors did not consider the complexity of crystal structure of both α-$La_2Mo_2O_9$ and β-$La_2Mo_2O_9$ phases and very easily pointed out on the cubic system without any prove, like for example analysis of the pseudo cubic reflection in the XRD patterns, which is an indicator of the cubic phase in $La_2Mo_2O_9$ molybdate.

We have started with Nd^{3+}-doped $La_2Mo_2O_9$ as described in two previous papers [44, 45] and have demonstrated that Nd^{3+}-doped monoclinic structure (α-

form) were observed for the concentration of Nd^{3+} ion up to 15 mol%. Pure cubic phase (β-form), necessary to get transparent ceramics, was obtained when the Nd^{3+} content had reached 50 mol%. However, in such a case of phases with high concentration of Nd^{3+} ions, unfavorable and very strong concentration quenching process takes place due to the clustering of Nd^{3+} ions and energy transfer by both down- and up-conversion processes. Continuing research, we have noticed that the partial substitution of Mo^{6+} ions by tungsten W^{6+} ones (ratio 1:1) can stabilize the cubic phase of mixed Yb^{3+}-doped La_2MoWO_9 molybdato-tungstate [46, 47]. We investigated also the influence of Yb^{3+} ions amount on $La_2Mo_2O_9$ structure, morphology and photoluminescence [48]. Detailed analysis of Yb^{3+}-doped $La_2Mo_2O_9$ shown that in some cases, as for 3 mol% of Yb^{3+}, it is cubic and could serve to produce transparent ceramics from the cubic nano-powders. It is worth to note that the Yb^{3+} luminescence in $La_2Mo_2O_9$ as Near Infra-Red (NIR) emitting optical material has never been reported up to now, so this is also one reason for our interest in this composition as laser material, but also because we can play with the presence of the $^2F_{7/2} \leftrightarrow {}^2F_{5/2}$ 0-phonon line of Yb^{3+} ion used as a structural probe in solids. The complexity of the $La_2Mo_2O_9$ crystal structure bring some difficulties in the interpretation of the spectroscopic results. Micro-crystalline samples obtained by high-temperature solid-state reaction characterized by higher crystallinity of material, and thus by more intense luminescence, were selected to perform the fundamental investigations of optical properties. Finally, the nano-powder obtained by the combustion method containing 3 mol% of Yb^{3+} ion was used to obtain Yb^{3+}-doped $La_2Mo_2O_9$ in the form of first translucent ceramics [48].

Recently we discovered that RE^{3+}-doped Y_6MoO_{12} molybdates easily crystallize in the cubic form and may be more beneficial relative to the solid solutions investigated by us [49]. Until now novel, yellow, brown and brick-red colored compositions activated by Sm^{3+}, Pr^{3+} or Nd^{3+} ions yttrium molybdates have been reported as high near infrared reflecting pigments due to their excellent optical property of reducing the heat build-up effectively [50–52]. A large number of rare earth based NIR refractive pigments are proposed as alternatives to traditional transition metal oxides pigments because of their low toxicity. Also a few articles on Eu^{3+}-doped Y_6MoO_{12} and mixed $Y_6Mo_{1-x}W_xO_{12}$, $Y_6(W,Mo)(O,N)_{12}$ or $Lu_6Mo(W)O_{12}$ phosphors have been reported recently [53–57]. The advantages of this matrices we can find also in the localization of the CT band shifted to the blue region with respect to the other molybdates or tungstates of tetragonal-coordinated $W(Mo)O_4$ groups. Indeed, the four-fold coordination (MO_4 groups; M = Mo, W) present in the scheelite-type structure shows the charge transfer bands (CTBs) of MO_4 groups located in the UV region, and thus near-UV or blue light cannot be utilized to excite rare earth activators through the host lattices. Compared with MO_4 groups, sixth-fold coordination (MO_6 groups) can efficiently absorb near-UV light by the ($O^{2-} \rightarrow M^{6+}$) CTBs and transfer the excitation energy to the activator [58]. These Eu^{3+}-doped compounds have been investigated in the frame of exploring of near-UV/blue light excited color-conversion phosphors in an expectation of obtaining white light with high color rendering index and low color temperature, namely,

warm white light. It is worth noting that the Yb^{3+} luminescence in Y_6MoO_{12} has never been reported before us and this is why we present solid solutions of this material as a very promising NIR emitting optical materials for phosphors and lasers with some hope to obtain them in the nearest future in the form of transparent ceramic due to their cubic structure.

In this review we would like to summarize some results on the Yb^{3+} ion activated cubic molybdates and molybdato-tungstates for optical transparent ceramics which have been presented as a lecture at the Erice's school. There are presented the detailed structural and spectroscopic studies performed by using complementary techniques as XRD, SEM with EDS, high-resolution low-temperatures absorption and emission with site selective excitation, which together brought very precious information. We are pointing out the advantages and disadvantages of the analyzed host lattices. Finally, we present also some results obtained for the first translucent ceramics.

17.2 Experimental Section

17.2.1 Sample Preparation

17.2.1.1 Synthesis of Yb^{3+}-Doped $La_2Mo_2O_9$

A series of micro-crystalline Yb^{3+}-doped $La_2Mo_2O_9$ molybdates with various concentrations of Yb^{3+} ion (x = 0, 0.5, 1, 2, 3, 4, 5, 6, 7, 8, 9, 10, 15 and 25 mol%) were successfully synthesized by a high-temperature solid-state reaction. The stoichiometric quantities of high purity commercial powders of La_2O_3, (99.999%, Stanford Materials), Yb_2O_3 (99.995%, Stanford Materials), MoO_3 (99.95%, Alfa Aesar) were used as initial reactants in this synthesis. Both rare-earth oxides were previously calcined at 850 °C in air in two 12-h heating stages to remove adsorbed moisture and carbon dioxide. The starting materials weighed in suitable molar proportion were mixed together and homogenized thoroughly by grinding in an agate mortar. All initial mixtures $Yb_2O_3/Y_2O_3/MoO_3$ were transferred into corundum crucibles and heated in air in the five stages: 600 °C/6 h, 700°C/6 h, 900°C/12 h, 1000°C/12 h and 1100°C/12 h. After each heating stage, Yb^{3+}-doped materials were slowly cooled to room temperature and then reground in an agate mortar with acetone for better reactivity.

The synthesis of Yb^{3+}-doped $La_2Mo_2O_9$ can be described by the following equation:

$$(1 - x/2)\ La_2O_{3(s)} + x/2\ Yb_2O_{3(s)} + 2\ MoO_{3(s)} = La_{2-x}Yb_xMo_2O_{9(s)} \tag{17.1}$$

17.2.1.2 Synthesis of Yb^{3+}-Doped La_2MoWO_9

The procedure performed for La_2MoWO_9 was very similar. However, the initial mixtures $Yb_2O_3/Y_2O_3/MoO_3/WoO_3$ were heated in air only in one stage at 1100 °C during 2 h. The micro-powder was obtained according to the reaction:

$$(1 - x/2)\ La_2O_{3(s)} + x/2\ Yb_2O_{3(s)} + MoO_{3(s)} + WO_{3(s)} = La_{2-x}Yb_xMoWO_{9(s)} \quad (17.2)$$

17.2.1.3 Synthesis of Yb^{3+}-Doped Y_6MoO_{12}

A series of micro-crystalline molybdates with chemical formula of $Y_{6\text{-}x}Yb_xMoO_{12}$ (later labelled as Yb^{3+}-doped Y_6MoO_{12}) with different concentration of optically active ion were synthesized by a high-temperature solid state reaction method. The concentration of the activator was set to 0.1, 1, 3, 5, 10, and 20 mol%, calculated in respect to Y^{3+} substitution. Commercial powders of Y_2O_3 (99.999%, Stanford Materials), Yb_2O_3 (99.995%, Stanford Materials), MoO_3 (99.95%, Alfa Aesar) were used as the starting reactants for synthesis of Yb^{3+}-doped Y_6MoO_{12} solid solutions. Before the synthesis, RE oxides were calcined at 850 °C, with two 12-h heating stages to remove adsorbed moisture and carbon dioxide. Weighed in appropriate molar ratios, the oxides were homogenized by grinding in an agate mortar. Next, as-prepared $Yb_2O_3/Y_2O_3/MoO_3$ mixtures were heated in corundum crucibles, in air, with 6-h annealing stages, and at temperatures from 550 to 750 °C. In next step, all samples were sintered with 12-h stages and at temperatures from 800–1000 °C. Finally, all ceramic materials were annealed at 1200, 1400, 1500 and 1550 °C for 6-h stages. After each heating stages the samples were cooled slowly down to ambient temperature, and for better reactivity, ground in an agate mortar. Several regrinding and heating sequences at the temperatures mentioned above were necessary to obtain appropriate and high-purity products. The synthesis of the solutions was started at a relatively low temperature (550 °C) due to the low melting point of MoO_3 (*ca.* 760 °C) and the possible mass loss caused by evaporation of this oxide. The phase composition of the samples was controlled by using powder X-ray diffraction (XRD). The pure and doped RE_6MoO_{12} phases can arise at 1500 °C. For this reason, it was absolutely necessary to apply so high temperature of annealing. The synthesis of samples under study can be described by the following equation:

$$(3\text{–}1/2x)\ Y_2O_3 + 1/2x\ Yb_2O_3 + MoO_3 = Y_{6-x}Yb_xMoO_{12} \quad (17.3)$$

17.2.1.4 Fabrication of Yb^{3+}-Doped $La_2Mo_2O_9$ and La_2MoWO_9 Translucent Ceramics

For the preparation of first translucent ceramics the cubic 3 mol% Yb^{3+}-doped $La_2Mo_2O_9$ and 3 mol% Yb^{3+}-doped La_2MoWO_9 nano-crystalline powders were used. This powders were prepared by combustion method according to previous paper [47]. Appropriate amounts of nano-powders was transferred to form and pressed under atmospheric pressure of 4 atm. during 5 min. Then, a white tablets was sintered at 1200 °C/6 h in vacuum atmosphere. In result a light yellowish (yellow-orange) (translucent ceramics, presented on the picture in the Sect. 17.4 of this paper, was obtained. Attempts to obtain transparent ceramics were carried out only for 3 mol% Yb^{3+}-doped $La_2Mo_2O_9$ and 3 mol% Yb^{3+}-doped La_2MoWO_9.

17.2.2 Apparatus

XRD Phase Analysis Room temperature (RT) powder XRD method was used to identify the phase purity and the crystal structure of solid solutions. X-ray diffraction patterns were collected over the angular range $2\Theta = 10–90°$ in continuous scanning mode with the scan rate of 0.008° per step on a D8 ADVANCE powder diffractometer with nickel-filtered Cu Kα radiation ($\lambda = 1.5418$ Å) and a Vantec detector, as well as on EMPYREAN II diffractometer (PANalytical) using Cu $K\alpha_{1,2}$ radiation ($\lambda = 1.5418$ Å) within $2\Theta = 10–70°$ range with a scan rate 0.008° per step and a counting time of 4 s per step. XRD patterns were analyzed by *HighScore Plus 4.0* software and lattice parameters were calculated using the least squares refinement procedure by *POWDER* software [59].

Density Measurements The density of samples under study was measured on a Ultrapycnometer 1000 Quantachrome Instruments (model Ultrapyc 1200e, USA) using argon (99.999%) as a pycnometric gas.

Scanning Electron Microscopy (SEM) The particle size and surface morphology of the Yb^{3+}-doped micro-powders and translucent ceramics were studied by scanning electron microscopy (SEM) using Hitachi S-3400N equipped with an energy dispersive X-ray spectroscopy EDS detector Thermo Scientific Ultra Dry. The powders were coated with thin gold alloy layer to facilitate conductivity, while the ceramics was analyzed without the gold coating.

Emission and Excitation Measurements The steady state emission spectra were measured using a SpectraPro 750 monochromator, equipped with a Hamamatsu R928 photomultiplier and a 1200 l/mm grating blazed at 500 nm. A 450 W xenon arc lamp was used as the excitation source. It was coupled with a 275 mm excitation monochromator which used a 1800 l/mm grating blazed at 250 nm. The excitation spectra were corrected for the excitation light intensity while the emission spectra were corrected for the instrument response. The measurements were taken at room

temperature (RT). **Site selective excitation and time resolved spectroscopy** (or Fluorescence Line Narrowing) was performed at 77 K in a nitrogen cryostat (or quartz dewar). A tuneable laser (EKSPLA OPO NT342B, 7 ns, 10 Hz) was used for scanning the excitation wavelength around 465 and 580 nm. The fluorescence was collected with an optical fiber and analysed with the help spectrometer equipped with a 1200 l/mm grating blazed at 500 nm, coupled to intensified charge coupled device (ICCD) camera (Shamrock 303 and iStar from Andor Technology).

Luminescence Decay Measurements The luminescence decay curves were recorded under pulsed laser excitation (OPO laser, EKSPLA NT342, 10 Hz, 7 ns), the fluorescence intensity around 1.06 μm being detected with a R1767 Hamamatsu photomultiplier through a HRS1 Jobin-Yvon monochromator equipped with a 1 μm blazed grating and coupled to a LECROY LT 342 digital oscilloscope. The luminescence decay curves were recorded at RT and 77 K.

17.3 Results and Discussion

17.3.1 Yb^{3+}-Doped $Y_2Mo_2O_9$ and Yb^{3+}-Doped Y_2MoWO_9 Micro-powders

17.3.1.1 Structural Analysis

As we reported in the articles devoted to $La_2Mo_2O_9$ molybdate activated by Nd^{3+} ions, dilanthanum molybdate with the formula of $La_2Mo_2O_9$ shows a reversible polymorphic transformation at 555 °C (determined during controlled heating of $La_2Mo_2O_9$ sample) from low-temperature α-phase (monoclinic structure) to high-temperature β-phase (cubic structure) [44, 45].

The monoclinic structure of $La_2Mo_2O_9$ phase with unit cell parameters: $a = 14.325(3)$ Å, $b = 21.482(4)$ Å, $c = 28.585(6)$ Å, β=90.40(3)°, V = 8796(3) Å^3, Z = 48, S.G. $P2_1$ was characterized based on small clear crystals by Evans et al. [60]. This structure is very complex and does not resemble the typical inorganic oxide due to the presence of 312 crystallographically independent atoms: 48 La, 48 Mo and 216 O. It corresponds to the 2 × 3 × 4 superstructure of the cubic structure of high-temperature $La_2Mo_2O_9$ phase. Both La^{3+} and Mo^{6+} cations have mixing oxygen coordination. The La^{3+} cations are found in irregular geometries containing different coordination numbers, between 6 and 12 oxygen anions, and 30 out of the 48 independent La^{3+} cations possess 9 oxygen anions. In turn, the Mo^{6+} cations occur in the three local coordination: tetrahedral, trigonal bipyramidal and octahedral.

The crystallographic data of cubic structure of high-temperature $La_2Mo_2O_9$ phase based on single crystal were presented by Alekseeva et al. [61]. The X-ray diffraction measurements were performed at 33 K to obtain the following unit-cell parameters: $a = 7.1377(2)$ Å, $\alpha=\beta=\gamma = 90°$, V = 363.64(2) Å^3, Z = 2, S.G.

$P2_13$. In contrast to the monoclinic structure, both of La^{3+} and Mo^{6+} coordination polyhedra are not be precisely determined because of partially occupied positions by the ions. The analysis of structure showed 15 oxygen anions surround La^{3+} cation and 7 oxygen anions are in the environment of Mo^{6+} cation. Moreover the interatomic distances between metal and oxygen vary from 2.3 to 2.93 Å for La-O and from 1.53- to 1.97 Å for Mo-O [62].

Hou et al. have also studied the cubic structure features of high-temperature $La_2Mo_2O_9$ modification using ab initio MD simulations. In contrast to previous results reported by Alekseeva, there were different data on the geometry optimization calculation. An important conclude of their research is that the all structure consists of mixture of coordinated cation sites. Molybdenum creates MoO_4 tetrahedra and MoO_5 trigonal bipyramids, while the lanthanum cations create much complex polyhedra, because La^{3+} cations are surrounded by seven or eight oxygen anions, forming LaO_7 and LaO_8 polyhedra. However, all Mo cations do not share common oxygens and are isolated by lanthanum polyhedra. In contrast to molybdenum polyhedra, there was noticed that three LaO_8 polyhedra and one LaO_7 polyhedra are connected together by sharing oxygen ions, forming complex network in three dimensions [63].

In case of Yb^{3+}-doped $La_2Mo_2O_9$ solid solutions, is expected that the Yb^{3+} ions occupy the same crystallographic positions as La^{3+} ones. The substitution of La^{3+} ions (1.10 Å for CN = 7 and 1.16 Å for CN = 8) by much smaller Yb^{3+} ones (0.925 Å for CN = 7, and 0.985 Å for CN = 8) and the same oxidation state (+3) does not require of a charge compensation and prevents to the formation of cationic holes.

Figure 17.1 shows the room temperature XRD patterns of the Yb^{3+}-doped samples obtained after the final sintering stage with the reference patterns of monoclinic (ICSD #172479) as well as cubic modification (ICSD #420672) of $La_2Mo_2O_9$ within the 2θ range of 10–70°.

If we look at XRD patterns from ICSD for the monoclinic (ICSD #174279) and the cubic (ICSD #420672) phases we could have an impression that that the positions of the diffraction lines for both phases are the same. However, the reflections for the monoclinic system have a more complex profiles. As an example in the insert of Fig. 17.1 we present the most informative pseudo-cubic [321] peak at 47Θ48° 2θ angle, which by change of the profile allows to determine the monoclinic (peak split into few components) or cubic (only one component of much broad and symmetrical peak) structure. The content of La_2O_3-MoO_3-Yb_2O_3 initial mixtures, total concentration of Yb^{3+} ions in final doped materials, calculated lattice parameters, calculated and experimental values of density for the identified Yb^{3+}-doped $La_2Mo_2O_9$ and Yb^{3+}-doped La_2MoWO_9 materials with detailed analysis of diffractograms were reported recently [46, 48]. It is observed that when the initial Yb^{3+} content is small, *i.e.* 0.5–2 mol%, the product of reaction between three metal oxides is only $La_{2-x}Yb_xMo_2O_9$ solid solution with monoclinic structure of $La_2Mo_2O_9$. We should not forget that Yb^{3+} ion (CN = 7 ionic radius – 0.925 Å, CN = 8 ionic radius – 0.985 Å) has much smaller ionic radius than La^{3+}

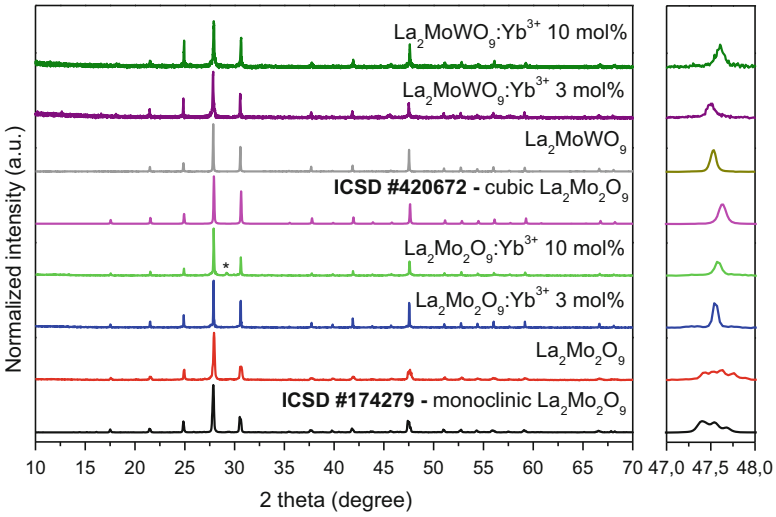

Fig. 17.1 X-ray powder diffraction patterns of monoclinic and cubic Yb^{3+} – doped molybdates and molybdato-tungstates

one (CN = 7 ionic radius – 1.10 Å and CN = 8 ionic radius – 1.16 Å). XRD measurements of the sample obtained by heating the mixture comprising initially 1 mol% of Yb_2O_3 (3 mol% Yb^{3+}, $x = 0.06$) show the presence of one solid phase, *i.e.* $La_{2-x}Yb_xMo_2O_9$ solid solution with cubic symmetry. At the concentration range over 4 mol% Yb^{3+}, two solid phases are found, *i.e.* cubic modification of $La_{2-x}Yb_xMo_2O_9$ and monoclinic Yb_2MoO_6 occurring in the samples on treatment. Starting from the sample with the concentration of 4 mol% Yb^{3+} the lattice parameters are very close to each other and to the *a* parameter calculated for cubic modification of $La_{2-x}Yb_xMo_2O_9$ ($x = 0.06$) [48]. An unexpected mixture of two phases: cubic molybdate of $La_2Mo_2O_9$ (ICSD #420672) and additional phase of Yb_2MoO_6 (ICSD #99574) is seen for the sample with concentration of Yb^{3+} equal 10 mol% (in Fig. 17.1 green line). The above observations clearly indicate that solubility limit of Yb^{3+} in $La_2Mo_2O_9$ is not higher than 4 mol%. Thus, in the case of obtained Yb^{3+}-doped materials it is observed that a substitution of La^{3+} ions by Yb^{3+} ones does not stabilize a cubic modification of $La_{2-x}Yb_xMo_2O_9$ within wide concentration range of dopant. It is only seen in the case of 3 mol% ($x = 0.06$). The experimental results show that for obtaining the Yb^{3+}-doped materials with cubic symmetry in all concentration range of activator by using the high-temperature solid-state reaction, the partial substitution of Mo^{6+} ions by W^{6+} ones is necessary.

17.3.1.2 Morphology and Particle Size by SEM Analysis

Figure 17.2 shows the SEM (Scanning Electron Microscope) micrographs of Yb^{3+}-doped $La_2Mo_2O_9$ molybdates with different content of the active ion. Due to the many stages of sintering at high temperature the grains formed micro-crystallites with a grain size in the range from 5 to even 15 μm. The overview pictures show that the good quality materials formed only for the materials containing small amount of activator. The powders with concentration of Yb^{3+} ions from 0.5 to 3 mol% are composed from homogeneous spherical shape of grains, with slight aggregation and a boundary between the microcrystals of powders clearly seen. Occasionally, on the surface of the grains one can see a few white grains of much smaller sizes of the order of several nanometers, very rich in Yb^{3+} ions, as indicated the EDS analysis. With increasing concentration of Yb^{3+} ions, the single particles are agglomerated into bigger clusters with irregular shape of micro-meter size. For higher concentration of Yb^{3+} ions the agglomerates form the sintered irregular blocks of size even 50–70 μm. However, at high magnification it is seen that on the surface of the big Yb^{3+}-doped $La_2Mo_2O_9$ grains, the second phase in form of cube-shaped crystals is created. The SEM micrographs and the energy dispersive X-ray (EDS) analysis indicate existing of two phases starting from 4 mol% of Yb^{3+} ions, thus morphology of Yb^{3+}-doped $La_2Mo_2O_9$ strongly depends on the amount of Yb^{3+} ions. From the Fig. 17.2 we see that the second phase occurs quite extensively, and the EDS analysis reveals very high content of Yb^{3+} ions in the cube-shaped crystals. The correlation of the results obtained from two applied methods (XRD patterns and SEM micrographs – EDS analysis) allows us supposed that this second Yb^{3+}- rich phase correspond to the monoclinic Yb_2MoO_6 phase, as postulated in the previous section (17.3.1.1 Structural analysis). Formation of the second phase is probably due to the small solubility limit of Yb^{3+} ions (3 mol%) in Yb^{3+} – doped $La_2Mo_2O_9$. The presence of La^{3+} ions in the results from EDS analysis is due to the measurement technique. The cube-shaped phase of Yb_2MoO_6 is located on the surface of Yb^{3+}-doped $La_2Mo_2O_9$, so electrons during analysis penetrate also the $La_2Mo_2O_9$ phase.

For the cubic Yb^{3+}-doped La_2MoWO_9 molybdato-tungstate micro-powders the phenomenon of second Yb_2MoO_6 phase formation was not observed [46].

17.3.1.3 Absorption Spectra

In order to investigate the absorption properties of Yb^{3+}-doped $La_2Mo_2O_9$, the measurements at room temperature and 4.2 K have been performed. As an example, in Fig. 17.3 we present the spectra obtained for 4 mol% of Yb^{3+} ion. High-resolution absorption spectra present four broad lines corresponding to $^2F_{7/2}(1) \rightarrow {}^2F_{5/2}$ (5,6,7) electronic transitions and to vibronic ones. The half-widths and positions of them practically do not change with decreasing the temperature: 1 → 5 (973.3 nm at RT, 972.5 nm at 4.2 K), 1 → 6 (944 nm at RT, and 946 nm at 4.2 K), 1 → 7 (926 nm at both temperature) and vibronic transitions at 963, 904 nm and 912 nm

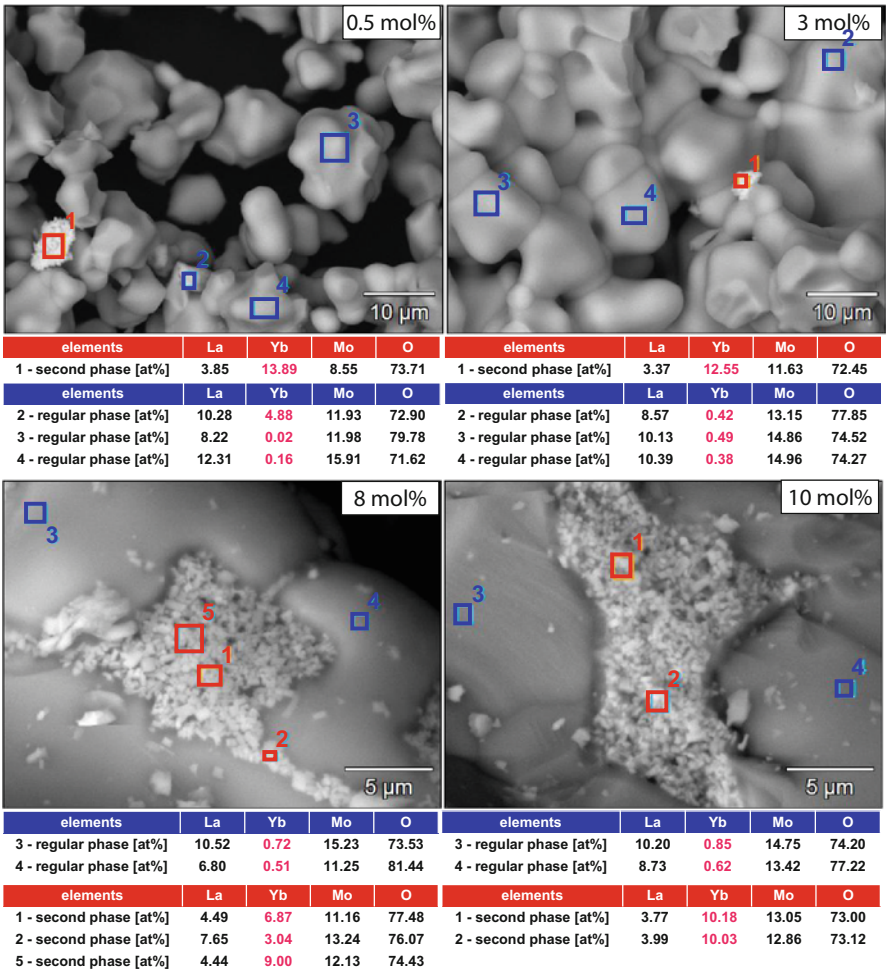

elements	La	Yb	Mo	O
1 - second phase [at%]	3.85	13.89	8.55	73.71

elements	La	Yb	Mo	O
2 - regular phase [at%]	10.28	4.88	11.93	72.90
3 - regular phase [at%]	8.22	0.02	11.98	79.78
4 - regular phase [at%]	12.31	0.16	15.91	71.62

elements	La	Yb	Mo	O
1 - second phase [at%]	3.37	12.55	11.63	72.45

elements	La	Yb	Mo	O
2 - regular phase [at%]	8.57	0.42	13.15	77.85
3 - regular phase [at%]	10.13	0.49	14.86	74.52
4 - regular phase [at%]	10.39	0.38	14.96	74.27

elements	La	Yb	Mo	O
3 - regular phase [at%]	10.52	0.72	15.23	73.53
4 - regular phase [at%]	6.80	0.51	11.25	81.44

elements	La	Yb	Mo	O
1 - second phase [at%]	4.49	6.87	11.16	77.48
2 - second phase [at%]	7.65	3.04	13.24	76.07
5 - second phase [at%]	4.44	9.00	12.13	74.43

elements	La	Yb	Mo	O
3 - regular phase [at%]	10.20	0.85	14.75	74.20
4 - regular phase [at%]	8.73	0.62	13.42	77.22

elements	La	Yb	Mo	O
1 - second phase [at%]	3.77	10.18	13.05	73.00
2 - second phase [at%]	3.99	10.03	12.86	73.12

Fig. 17.2 SEM micrographs and EDS elemental analysis of Yb^{3+}-doped $La_2Mo_2O_9$ molybdates

at RT and 910 nm at 4.2 K. When the temperature decreases, the absorption lines should narrow. In this case only broad well-formed 0-phonon is slightly narrowing. Broad lines still recorded at 4.2 K suggest a large disordering of active ions in the structure. We already proposed the existence of such a disorder in the structure for the similar compositions of $La_2Mo_2O_9$ dilanthanum dimolybdate doped with Nd^{3+} ions as well as for Yb^{3+}-doped mixed La_2MoWO_9 molybdato-tungstates [32, 37]. Here, as we can see from the Table 17.1 [42] the difference between the ionic radii of La^{3+} and Yb^{3+} is bigger than in case of La^{3+} and Nd^{3+} ions, so the disorder in the framework may also be bigger.

In turn, not presented here, room temperature absorption spectra recorded for molybdates with cubic structure (3–10 mol% Yb^{3+}-doped $La_2Mo_2O_9$) are similar

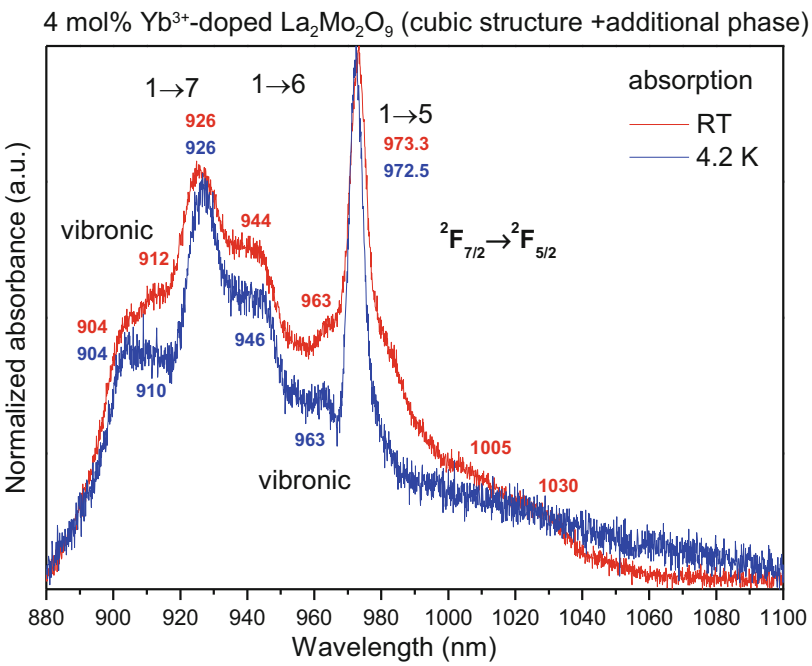

Fig. 17.3 Absorption spectra of 4 mol% Yb^{3+}-doped $La_2Mo_2O_9$ molybdates recorded at RT and 4.2 K

Table 17.1 Ionic radii of La^{3+}, Nd^{3+} and Yb^{3+} according to CN coordination number [62]

	La^{3+} [Å]	Nd^{3+} [Å]	Yb^{3+} [Å]
CN = 7	1.1	–	0.925
CN = 8	1.16	1.109	0.985
CN = 9	1.216	1.163	1.042

as for monoclinic samples (0.5–2 mol%) and present the broad, well-separated and contain only one component of 0-phonon line (1 → 5). Nevertheless, the calculated value of full width at half maximum (FWHM) is equal 196.5 cm^{-1} (3 mol% of Yb^{3+}) [48]. It may be due to the second, hidden component which suggests the multisite character of Yb^{3+} ions. These results are consistent with studies on Yb^{3+}-doped La_2MoWO_9, which demonstrated also one and broad 0-phonon line, most probably related to the existence of two main LaO_8 and LaO_7 polyhedra in the structure of La_2MoWO_9 molybdato-tungstates [46, 47]. In the whole series of Yb^{3+}-doped $La_2Mo_2O_9$ molybdates with the cubic structure the values of the FWHM of 0-phonon line systematically decrease with increasing the concentration of Yb^{3+} ion from 196.5 cm^{-1} (3 mol%) to 106 cm^{-1} (10 mol%). The intensity of the lines corresponding to 1 → 7 and 1 → 6 transitions in the 875–960 nm spectral range increases with higher concentration of Yb^{3+} up to 10 mol% of Yb^{3+} ions [48]. For high concentration of the activator the intensity of the line at 925 nm

corresponds to the 1 → 7 electronic transition is almost equal to intensity of the 0-phonon line. Moreover, the room temperature absorption spectra revealed the additional two additional absorption bands correspond to transition from second (2) and third (3) Stark sublevel of the ground state $^2F_{7/2}$ to the lowest higher sublevel (5) of the excited state $^2F_{5/2}$, which are located at 1006 nm (2 → 5) and 1030 nm (3 → 5), respectively.

To see the effect of introduction of W^{6+} ion into the $La_2Mo_2O_9$ matrix on the optical properties we present in Fig. 17.4 the room (Fig. 17.4a) and low (Fig. 17.4b) absorption spectra of 8 mol% Yb^{3+}-doped $La_2Mo_2O_9$ (cubic + additional phase) and 10 mol% Yb^{3+}-doped La_2MoWO_9 (cubic phase). Comparison of two similar systems: Yb^{3+}-doped $La_2Mo_2O_9$ molybdates and Yb^{3+}-doped mixed La_2MoWO_9 molybdato-tungstates lead to conclusion that at room and low temperatures, the absorption lines for $La_2Mo_2O_9$ are slightly shifted into higher energies and also that for La_2MoWO_9 molybdato-tungstates the spectra are less structured, so the larger disorder in the structure caused by substitution of one Mo^{6+} ion (i.r. – 0.59 Å) by one W^{6+} one (i.r. – 0.6 Å) is well seen. A big difference is the spectral shape observed for Yb^{3+}-doped $La_2Mo_2O_9$ and Yb^{3+}-doped La_2MoWO_9 especially at 4.2 K is a consequence of the presence of stoichiometric Yb_2MoO_6 second phase in 8 mol% Yb^{3+}-doped $La_2Mo_2O_9$. In both cases, the most intense absorption band is 0-phonon line with one broad distinct component, much broader for La_2MoWO_9. The values of full width at half maximum (FWHM) of 0-phonon line are quite different, around two times bigger for Yb^{3+}-doped $La_2Mo_2WO_9$ (97 cm^{-1}) than in

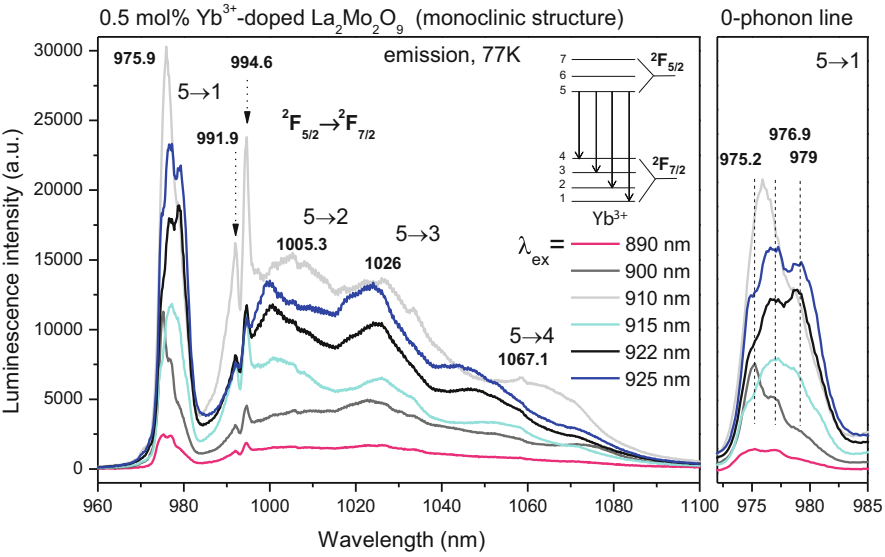

Fig. 17.4 Site selective emission spectra of 0.5 mol% Yb^{3+}-doped $La_2Mo_2O_9$ solid solution, measured at 77 K under different excitation wavelengths of the Ti-sapphire laser

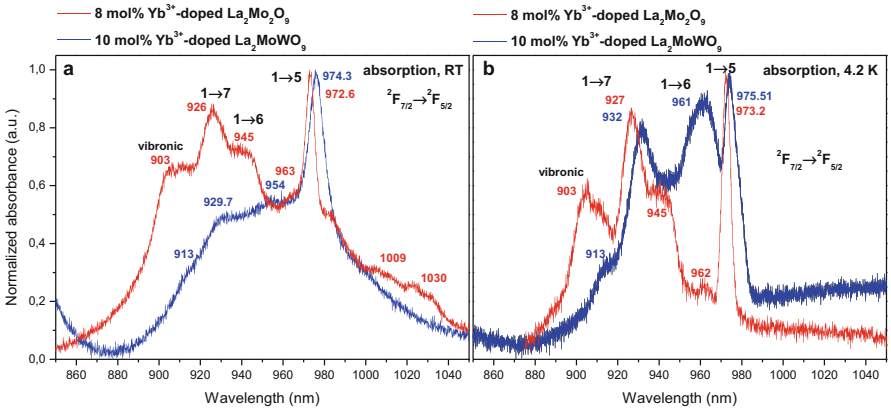

Fig. 17.5 Room (**a**) and low temperature (**b**) absorption spectra of 8 mol% Yb^{3+}-doped $La_2Mo_2O_9$ (cubic structure + additional phase, red line) and 10 mol% Yb^{3+}-doped La_2MoWO_9 (cubic structure, blue line)

case of Yb^{3+}-doped $La_2Mo_2O_9$ (56 cm^{-1}). Based on the results, it can be concluded that the partial substitution of Mo^{6+} ion by W^{6+} once in Yb^{3+}-doped La_2MoWO_9 leads to larger disorder in the structure, although the ionic radii of the two transition metals is quite similar.

17.3.1.4 Emission Spectra

Presented in Figs. 17.5 and 17.6 site selective emission spectra recorded by using a tunable Ti-Sapphire laser were used to determine the spectroscopic properties of Yb^{3+}-doped $La_2Mo_2O_9$ materials and to compare the differences in photoluminescence properties of molybdates crystallizing in the monoclinic (0–2 mol%) and the cubic system (3–10 mol% Yb^{3+}). On the low temperature emission spectra of 0.5 mol% Yb^{3+}-doped $La_2Mo_2O_9$ with monoclinic structure (Fig. 17.5) it is easy to notice the complex structure of emission bands in the near infrared region 970–1090 nm. The most intense is called 0-phonon line and corresponds to the 5 → 1 transition in resonance with the 1 → 5 absorption line. This line is used as a reference for the spectroscopy of Yb^{3+}-doped materials. Only one component of the 0-phonon line is expected at low temperature for the same crystallographic sites of Yb^{3+} ions in the structure. In Fig. 17.5 with changing the excitation wavelengths from 890 nm to 925 nm it is observed here that the 0-phonon line splits into three components located at around 975.2 nm, 976.9 nm and 979 nm. These results indicate the different distribution of Yb^{3+} ions in the monoclinic structure of molybdates what is strongly related with crystal structure discussed in Sect. 17.3.1.1: According to Evans the La^{3+} cations are found in irregular geometries containing different coordination numbers, between 6 and 12 oxygen anions, and 30 out of the 48 independent La^{3+} cations possess coordination number 9. In

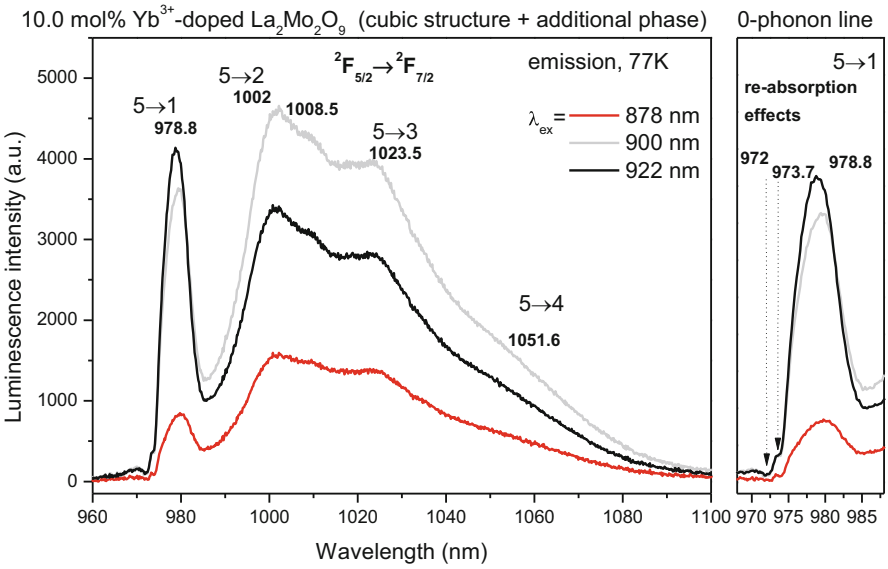

Fig. 17.6 Site selective emission spectra of 10 mol% Yb^{3+}-doped $La_2Mo_2O_9$ molybdate, measured at 77 K under different excitation wavelengths of the Ti-sapphire laser

turn, the Mo^{6+} cations occur in the three local coordination: tetrahedral, trigonal bipyramidal and octahedral [60]. Let's remind that in the monoclinic Nd^{3+}-doped $La_2Mo_2O_9$ obtained by us, at least two types of Nd^{3+} sites have been assigned with two coordination numbers of LaO_7 and LaO_8 [44, 45].A reasonable assignment might be that Yb^{3+} dopant reveals another coordination number like for example LaO_9, according to Evans possible to exist in this complex structure [60].

Despite the 0-phonon line, on the emission spectra of Yb^{3+} ions are expected three other emission bands corresponding to $^2F_{5/2}$ (5) → $^2F_{7/2}$ (2,3,4) electronic transitions. Usually they show the highest intensities with the electronic transitions than vibronic transitions. In case of emission spectra of monoclinic molybdates three expected intense lines with attributed transitions of Yb^{3+} ions are located at 1005.3 nm (5 → 2), 1026 nm (5 → 3) and 1067 nm (5 → 4) nm, respectively. Additionally, the two narrow components of emission lines at 991.9 and 994.6 nm are only recorded in the sample containing 0.5 mol% and more visible under $\lambda_{ex} = 910$ nm from the tunable Ti-sapphire laser. At this moment it is hazardous to assign them to Yb^{3+} ion and might be associated with an impurity only present in this specific sample. The photoluminescence intensity increases rightly with the change of excitation wavelengths from 890 nm to 925 nm in agreement with the profile of the absorption lines in Fig. 17.4.

Moreover, a continuous shift of the emission line corresponding to 5 → 4 transition occurs by changing excitation wavelength from 925 nm to 890 nm. This is another probe of the presence of multisites inside the molybdate lattice.

The emission spectra at low temperature of 10 mol% Yb^{3+}-doped $La_2Mo_2O_9$ by pumping with Ti-sapphire laser are presented in Fig. 17.6. In case of molybdates

with cubic structure are observed much broader emission lines with clearly noticeable positions at 978.8 nm (5 → 1), 1002 nm (5 → 2), 1023.5 nm (5 → 3) and 1051.6 nm (5 → 4).

The shape and the number of emission lines stay the same with changing the excitation wavelengths. The dominant features of the emission spectra recorded under laser diode excitation $\lambda_{ex} = 878$ and 900 nm are much intense emission lines attributed to 5 → 2 and 5 → 3 transitions than the 0-phonon line. We think that re-absorption phenomenon of the 0-phonon line 5↔1 occurs largely in such case. This results indicate evident differences for cubic molybdates from the monoclinic structure. Although the 0-phonon line is not split, the calculated value of full width at half maximum (FWHM) of this line is large, around 80.3 cm^{-1}, which indicates a distribution of un-equivalent sites. Moreover, the 0-phonon line has asymmetrical shape which is the most visible under $\lambda_{ex} = 900$ nm and 922 nm by pumping with a tuneable Ti-sapphire laser, leading to the hypothesis of two or three main environments of Yb^{3+} ions in this cubic lattice. Additionally, another re-absorption effect is observed on the emission spectra of Fig. 17.6 at 972 nm. It is probably the result of the high concentration of Yb^{3+} ions in Yb_2MoO_6 as seen in Fig. 17.2 for the morphology study.

We wanted to know the concentration dependence of Yb^{3+} ions on photoluminescence properties of molybdates and then we have recorded the low temperature emission spectra under the same laser diode excitation at $\lambda_{ex} = 405$ nm into the charge transfer band of the molybdate group (Figs. 17.7 and 17.8).

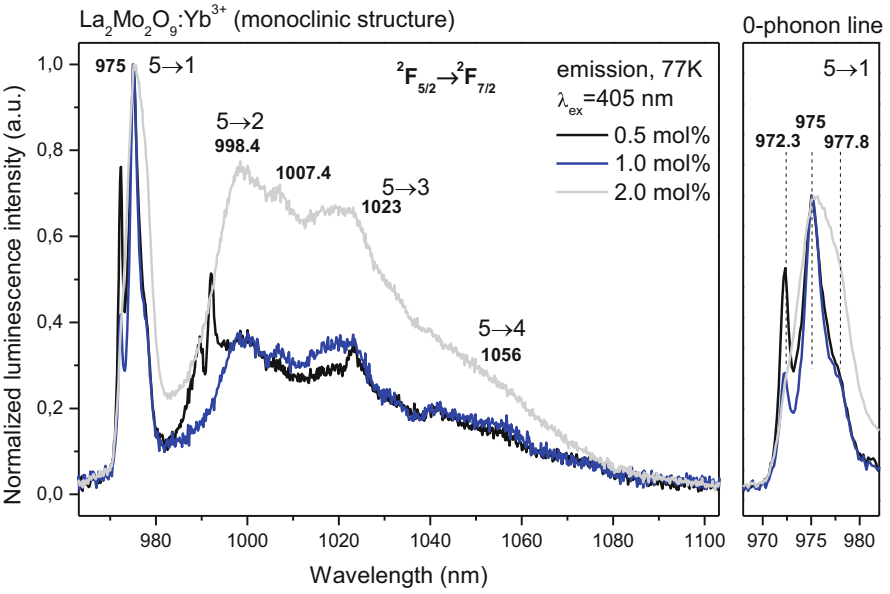

Fig. 17.7 Emission spectra of $La_2Mo_2O_9:Yb^{3+}$ 0.5, 1 and 2 mol% solid solutions crystallizing in the monoclinic system, measured at 77 K under laser diode excitation $\lambda_{ex} = 405$ nm into the charge transfer band of the molybdate group

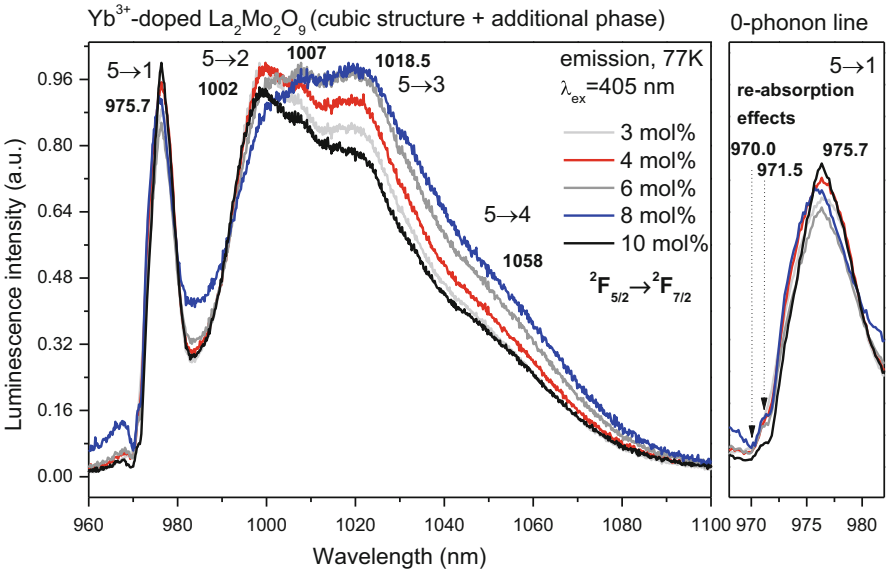

Fig. 17.8 Emission spectra of $La_2Mo_2O_9$:Yb^{3+} 3–10 mol% materials crystallizing in the cubic system, measured at 77 K under laser diode excitation $\lambda_{ex} = 405$ nm into the charge transfer band of the molybdate group. The values of wavelengths are mentioned for 8 mol% of Yb^{3+}

The 0.5 mol% of Yb^{3+}-doped $La_2Mo_2O_9$ molybdate with monoclinic structure shows two abnormal additional lines located at 989.6 nm and 992.1 nm which are still noticeable, under the laser diode excitation at $\lambda_{ex} = 405$ nm. As only this 0.5 mol % is concerned we have observed these two lines belong to a stoichiometric Yb_2MoO_6 phase characterized by the smallest white points, less than 1 μm, in the SEM photo of Fig. 17.5. The splitting of the 0-phonon line into three components (972.3 nm, 975 nm and 977.8 nm) are visible only for the lowest concentrations 0.5 and 1 mol% of Yb^{3+}-doped $La_2Mo_2O_9$ molybdates. However, the profile of this 0-phonon line is questionable in the following way. Instead to assign the sharp line at 972.3 nm to one component belonging to one special site symmetry or polyhedral coordination, we also can imagine there is a hole between 972.3 and 975 nm due to the reabsorption from the Yb^{3+} rich phase as can be seen in Fig. 17.2.

It should be a way to measure the absorption line of this Yb^{3+} segregation in the sample. In such hypothesis, it seems we can keep the resolution of three components of the 0-phonon line in Fig. 17.7 connected with three polyhedra in the monoclinic structure as already interpreted previously from the absorption spectra. When concentration of Yb^{3+} ions increases, the structured shape of the 0-phonon line disappears in the new cubic structure. Moreover, the large full width at half maximum (FWHM) of this line equals to 77.6 cm^{-1} suggests at least two or three slightly un-equivalent crystallographic sites occupied by the Yb^{3+} in substitution of La^{3+} ions of the cubic phase.

Based on the results, both monoclinic and cubic structures are pointed out in Yb^{3+}-doped $La_2Mo_2O_9$ molybdates. The substitution of Yb^{3+} ions on several types of La^{3+} sites causes the broadening of all emission lines suggesting a disordering of the Yb^{3+} ions in the host structure. The spectral resolution of the monoclinic phase is much higher than the cubic one. More especially, three main configurations of sites are detected in the monoclinic phase and most probably in the cubic phase which might be connected with three coordination numbers.

17.3.1.5 Some Comparison Between Cubic Structure of Yb^{3+}-Doped $La_2Mo_2O_9$ and Yb^{3+}-Doped Mixed La_2MoWO_9

In order to compare spectroscopic properties of two quite similar cubic systems: Yb^{3+}-doped $La_2Mo_2O_9$ and Yb^{3+}-doped La_2MoWO_9 were set together low and room temperature emission spectra recorded under Ti-sapphire laser (Fig. 17.9). For both samples, the most intense emission broad line on emission spectra corresponds to the similar 0-phonon line ($^2F_{5/2}$ (5) $\rightarrow$ $^2F_{7/2}$ (1) transition). The calculated value of full width at half maximum (FWHM) of the 0-phonon line is around 73.7 cm^{-1} for 3 mol% Yb^{3+}-doped $La_2Mo_2O_9$ and 72.2 cm^{-1} for 3 mol% Yb^{3+}-doped La_2MoWO_9, which suggests multisite disordered distribution of Yb^{3+} ions in both of structures. The room temperature and 77 K emission spectra shows weakly

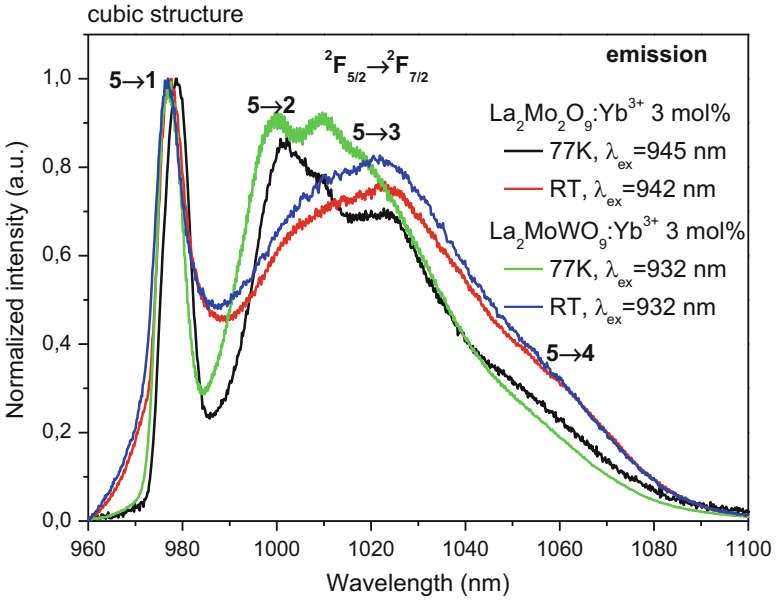

Fig. 17.9 Emission spectra of 3 mol% Yb^{3+}-doped $La_2Mo_2O_9$ and 3 mol% Yb^{3+}-doped La_2MoWO_9 solid solutions under selected excitation lines of the Ti-sapphire laser

separated broad emission bands. Successfully, along with the temperature drop to 77 K, the three emission bands located at 1000 nm (5 → 2), 1020 nm (5 → 3) and 1060 nm (5 → 4) for Yb^{3+}-doped La_2MoWO_9 and 1000.8 nm (5 → 2), 1024.4 nm (5 → 3) and 1047.8 nm (5 → 4) for Yb^{3+}-doped $La_2Mo_2O_9$ were observed.

17.3.1.6 Yb^{3+} Energy Level Diagram in $La_2Mo_2O_9$

In order to evaluate the crystal field splitting of $^2F_{5/2}$ and $^2F_{7/2}$ multiplets of Yb^{3+} ions in Yb^{3+}-doped $La_2Mo_2O_9$ is recorded low temperature absorption spectra (4.2 K) and emission spectra (77 K). The low temperature measurements are necessary to determine exact location of absorption and emission lines in contrast to the room temperature measurements which are not structured enough.

The energy levels scheme of Yb^{3+} ion in $La_2Mo_2O_9$ was drawn in Fig. 17.10. The value of total splitting levels equal 10,795 cm^{-1} for 8 mol% Yb^{3+}-doped $La_2Mo_2O_9$:Yb^{3+} is slightly bigger then 10,730 cm^{-1} in case of 10 mol% Yb^{3+}-doped La_2MoWO_9. The partial substitution of Mo^{6+} ions by W^{6+} ones (in ratio 1:1) promote a bit smaller splitting of multiplets of Yb^{3+} ions.

As can be seen from the Figs. 17.11 and 17.12, the position of the 0-phonon line on absorption and emission spectra are not the same. One most probable interpretation of this evident difference is the re-absorption effect associated with the resonance of absorption and emission lines. Two reasons can be involved: first, the presence of the second Yb_2MoO_6 phase with high concentration of Yb^{3+} ions giving rise to a hole in the 0-phonon line. Secondly, inside the main structure, where

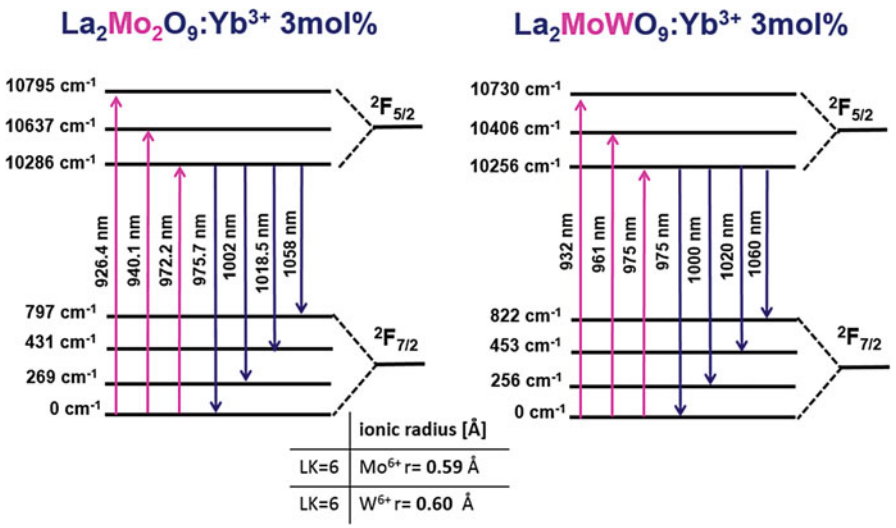

Fig. 17.10 Low temperature Stark splitting levels of Yb^{3+} ions calculated from the experimental data

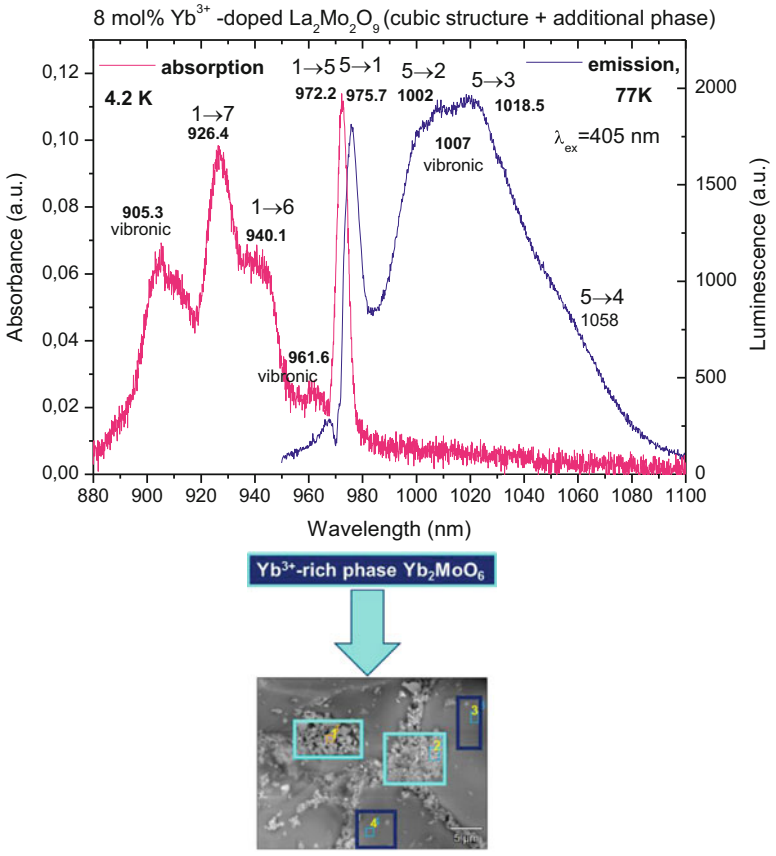

Fig. 17.11 Superposition of the absorption spectra at 4.2 K, emission spectra at 77 K of 8 mol% Yb^{3+}-doped $La_2Mo_2O_9$ cubic molybdate under laser diode excitation $\lambda_{ex} = 405$ nm (CT band)

multisites occur, a deformation of the profile of the 0-phonon line emission spectrum showing an overlapping between the absorption line of one of the three centers with the total emission spectrum.

Additionally, to compare the Stark splitting levels of Yb^{3+} ions and also re-absorption phenomena in $La_2Mo_2O_9$ and La_2MoWO_9 [47, 48] was reminded the low temperature superposition of absorption and emission spectra for 10 mol% Yb^{3+}-doped La_2MoWO_9 (Fig. 17.12).

17.3.1.7 Decay Analysis

Figure 17.13 presents collected decay profiles of Yb^{3+}-doped $La_2Mo_2O_9$ series of molybdates with large range of activator concentration (0.5–10 mol% Yb^{3+}) recorded at room temperature. The decay times were recorded under pulsed OPO

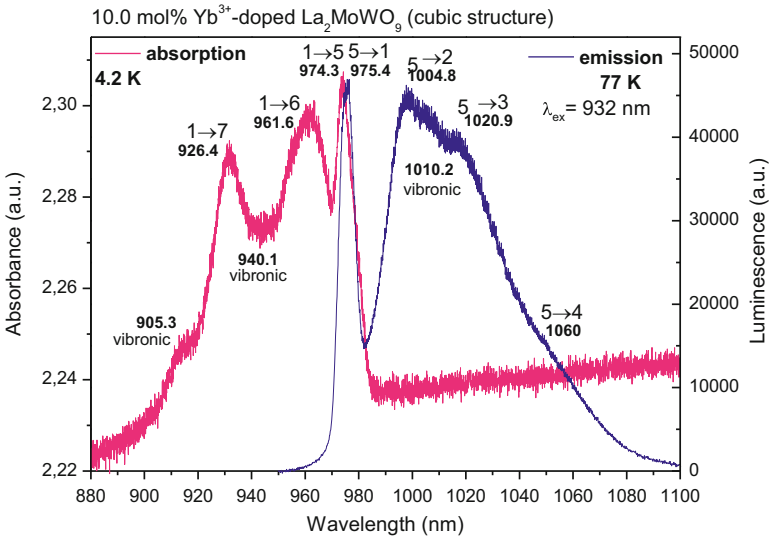

Fig. 17.12 Superposition of the absorption spectra at 4.2 K, emission spectra at 77 K of 10 mol% Yb^{3+}-doped mixed La_2MoWO_9 cubic molybdato-tungstates under Ti-sapphire laser excitation

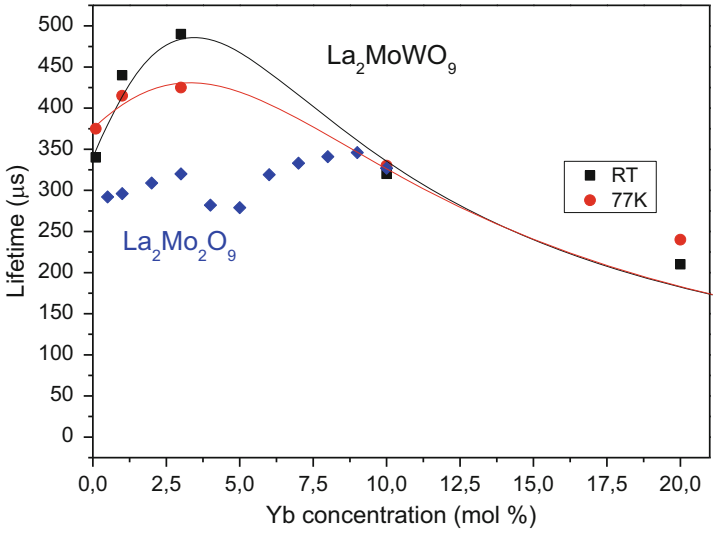

Fig. 17.13 Comparative concentration dependence of experimental decay times in Yb^{3+}-doped $La_2Mo_2O_9$ and Yb^{3+}-doped La_2MoWO_9 with different concentration of Yb^{3+} ions

laser laser pulsed excitation under $\lambda_{ex} = 975$ nm by monitoring $^2F_{5/2} \rightarrow {}^2F_{7/2}$ luminescence at $\lambda_{em} = 1030$ nm for the Yb^{3+}-doped $La_2Mo_2O_9$. These decays are considered as exponential profiles with an excellent approximation. Only the

points for the first μs deviate from the exponential as a result of an energy transfer between multisite Yb^{3+} ions. The values of the experimental lifetimes strongly depend on amount of Yb^{3+} ions as shown in Fig. 17.13. Among the whole series a slight increase of decay times is observed with approaching to 320 μs for 3 mol% Yb^{3+}. Then, the clearly visible reduction of value lifetimes is noticed for 4 and 5 mol%, which may be caused by the appearance of a new cubic phase. Above 5 mol% of Yb^{3+} ions, the decay lifetimes increase again from 319 μs up to 346 μs related to 6 and 9 mol% and increase again up to the slightest reduction to 327 μs for 10 mol%. There is evident correlation between the structural change from the monoclinic form ($Yb^{3+} \leq 2$ mol%) to the cubic form ($Yb^{3+} \geq 3$ mol%) and the decay lifetimes. An increase of Yb^{3+} ions contributes to the resonant diffusion process between the Yb^{3+} ions in all compounds and manifests as self-trapping phenomenon so that Fig. 17.13 shows the same behavior of the self-trapping effect for the two phases till 10 mol% of Yb^{3+} ions. The change of monoclinic and cubic structures indicates irregular changes of lifetimes has been compared with Yb^{3+}-doped $La_2Mo_2WO_9$ solid solutions which was described by the two usual phenomena of self-trapping effect and self-quenching effect [47]. Respectively, for the same activator concentrations are noticeable much longer decay lifetimes for Yb^{3+}-doped La_2MoWO_9 than for Yb^{3+}-doped $La_2Mo_2O_9$ solid solutions. It can suggest less number of resonant transitions of the $^2F_{5/2} \leftrightarrow {}^2F_{7/2}$ 0-phonon line and so shorter distances of light between the grains of Yb^{3+}-doped $La_2Mo_2O_9$: solid solutions.

17.3.1.8 Comparative Analysis of 3 mol% Yb^{3+}-Doped $La_2Mo_2O_9$ and 3 mol% Yb^{3+}-Doped La_2MoWO_9 Ceramics

First translucent ceramics of 3 mol% Yb^{3+}-doped $La_2Mo_2O_9$ and 3 mol% Yb^{3+}-doped La_2MoWO_9 ceramics have been successfully fabricated. The comparison turns out in favor of Yb^{3+}-doped mixed La_2MoWO_9. The structural and spectroscopic differences are also significant for these materials. Figure 17.14 presents SEM images with the EDS elemental analysis performed for 3 mol% Yb^{3+}-doped $La_2Mo_2O_9$ and 3 mol% Yb^{3+}-doped La_2MoWO_9 micro-ceramics sintered at 1200 °C/6 h in vacuum. For both cases the images indicate inhomogeneous morphology consisted of quite large grains with circular shape and much smaller, white points mostly accumulated at the grain boundaries (Fig. 17.21). According to the EDS analysis, the white points contain higher amount of Yb^{3+} ions than at the grains surface. The identification of this additional phase (white points) is very difficult due to the lack in crystallographic data base of standard corresponding to this phase. The performed analysis of morphology for both ceramics shows the troubles with obtaining transparent ceramics contained only one pure phase of Yb^{3+}-doped $La_2Mo_2O_9$ or Yb^{3+}-doped La_2MoWO_9. From Fig. 17.14 we see that La_2MoWO_9 ceramics is less yellow and characterized by better translucency.

Figure 17.15 presents comparison of room temperature and 4.2 K absorption spectra of Yb^{3+}-doped $La_2Mo_2O_9$ and Yb^{3+}-doped La_2MoWO_9 ceramics pre-

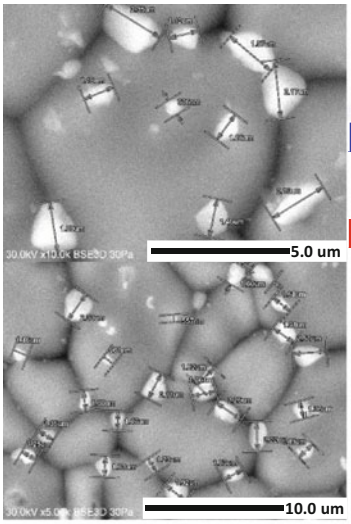

$La_2Mo_2O_9$: Yb^{3+} 3 mol% ceramics

elements	La	Yb	Mo	O
regular grain [at%]	11.20	0.28	15.16	73.36
regular grain [at%]	11.71	0.41	15.75	72.13
elements	**La**	**Yb**	**Mo**	**O**
white point [at%]	9.84	4.94	14.07	71.16
white point [at%]	8.80	3.54	12.84	74.81

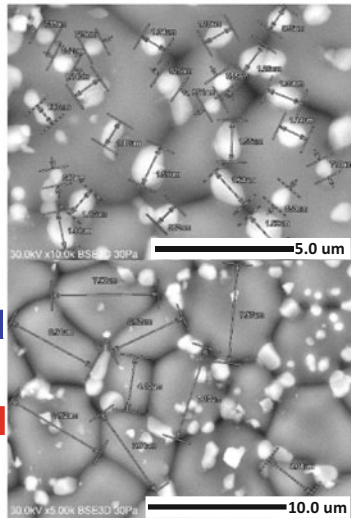

La_2MoWO_9:Yb^{3+} 3 mol% ceramics

elements	La	Yb	Mo	W	O
regular grain [at %]	10.79	1.03	7.60	6.85	73.74
regular grain [at %]	11.63	1.19	7.84	7.35	71.99
elements	**La**	**Yb**	**Mo**	**W**	**O**
white point [at %]	7.71	11.73	3.78	6.27	70.51
white point [at %]	8.01	9.67	4.41	6.25	71.66

Fig. 17.14 SEM images with the EDS elemental analysis performed for 3 mol% $Yb3^{3+}$-doped $La_2Mo_2O_9$ and 3 mol% Yb^{3+}-doped Yb^{3+}-doped La_2MoWO_9 micro-ceramics sintered at 1200 °C/6 h in vacuum

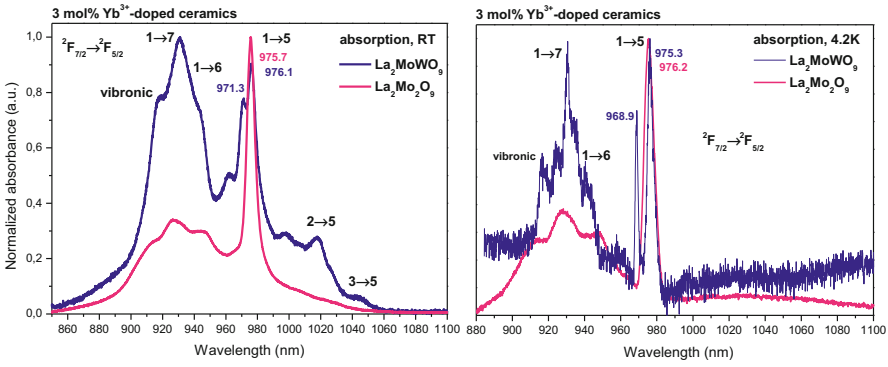

Fig. 17.15 Room and low temperature (4.2 K) absorption spectra of 3 mol% Yb^{3+}-doped $La_2Mo_2O_9$ and 3 mol% Yb^{3+}-doped La_2MoWO_9 sintered micro-ceramics

pared in the same annealing conditions at 1200 °C/6 h in vacuum. The room temperature absorption spectra reveals clearly visible differences of shape and number of components in the 850–1100 nm spectral range. Going to the low temperature absorption spectra, the differences are more pronounced. Only in case of Yb^{3+}-doped La_2MoWO_9, the intense 0-phonon line (1 → 5 transition) has two components, one at 968.9 nm at 4.2 K caused by the presence of the stoichiometric Yb_2MoO_6 in white points of Fig. 17.14 (11.73 at% and 9.67 at.% respectively) and another one at 976.2 nm at 4.2 K in the regular phase of Yb^{3+}-doped La_2MoWO_9. Therefore, on absorption spectra of Yb^{3+}-doped $La_2Mo_2O_9$ is visible only one component of 0-phonon line at 976.2 nm at 4.2 K. It is worth note that the 0-phonon line is relatively wide and a full width at half maximum (FWHM) equals to 72 cm^{-1} for molybdate and 44 cm^{-1} for molybdato-tungstate system. It may be suggest different distribution of the crystallographic Yb^{3+} sites in both structures. Additionally, even at low temperature absorption bands of Yb^{3+}-doped La_2MoWO_9 are more structured by existence of additional components primarily in the 900–970 nm spectral range.

The luminescence properties of 3 mol% Yb^{3+}-doped $La_2Mo_2O_9$ and 3 mol% Yb^{3+}-doped La_2MoWO_9 ceramics were investigated by using selective lines of Ti-sapphire laser in Fig. 17.16. The spectra were measured both at room and 77 K. As we can see, the common graph of emission spectra for Yb^{3+}-doped $La_2Mo_2O_9$ revealed mostly the same shape emission lines recorded at low temperature by changing the excitation wavelength and quite similar emission spectra at room temperature with the most intense and broad 0-phonon line at 977 nm as well as weakly resolved (5 → 2, 5 → 3, 5 → 4) emission lines in the 980–1080 nm spectral region. In contrast to that, the low temperature (77 K) emission spectra of 3 mol% Yb^{3+}-doped La_2MoWO_9 demonstrated the splitting of 0-phonon line into two components at 975 nm and 978 nm that affirmed the multisite character of Yb^{3+} ions most probably related to the two main YbO_7 and YbO_8 polyhedra.

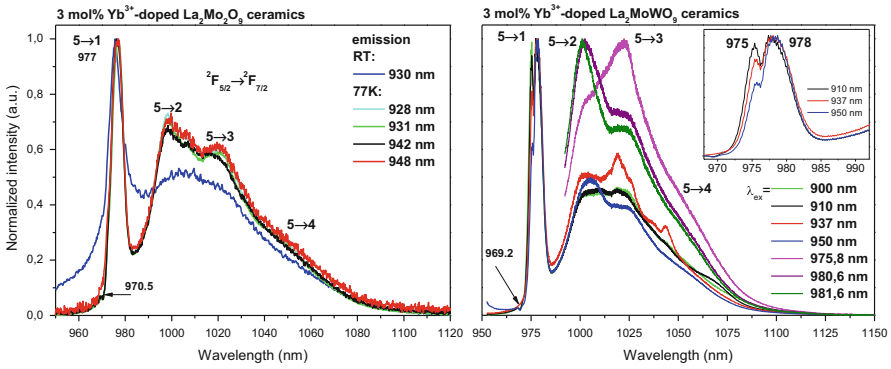

Fig. 17.16 Site selective emission spectra of 3 mol% Yb^{3+}-doped $La_2Mo_2O_9$ and 3 mol% Yb^{3+}-doped La_2MoWO_9 sintered micro-ceramics, measured under different excitation lines of the Ti-sapphire laser

Also changes in the intensity ratio of the emission lines strongly dependent on the excitation wavelengths. Additionally, the emission spectra of 3 mol% Yb^{3+}-doped La_2MoWO_9 includes one hole at 969.2 nm as signature of the reabsorption line corresponding to the additional 0-phonon line in the absorption spectra at 4.2 K presented in Fig. 17.15. This absorption line is associated with the unknown tetragonal Yb^{3+}-rich phase, which is observed as white points on the grain boundaries in Fig. 17.14 [46, 47]. In the case of the excitation line at 937 nm, we observed more than three bands in the range from 990 to 1100 nm, which should correspond to transitions from the lowest Stark level of the $^2F_{7/2}$ excited state (5) to Stark levels 2, 3, or 4. The multiplicity of emission lines point out a multisite character of the samples.

17.3.1.9 Conclusion for Yb^{3+}-Doped $La_2Mo_2O_9$/Mixed La_2MoWO_9 Cubic Materials

The structural studies for the first group: $La_2Mo_2O_9$ activated by Yb^{3+} dopants from 0.5 mol% to 25 mol% reveal the low solubility limit of 3 mol% Yb^{3+} ions in the $La_2Mo_2O_9$ host lattice. A small quantity of active ions ($\leq$2 mol% of Yb^{3+}) leads to obtain the pure monoclinic structure, while when the amount of Yb^{3+} ions is above 3 mol%, the mixture of two phases, the cubic structure of Yb^{3+}-doped $La_2Mo_2O_9$ and the additional phase of monoclinic stoichiometric Yb_2MoO_6, was detected. Depending on the concentration of Yb^{3+} ions, the obtained molybdates have different morphology. If the amount of dopant is less than 3 mol% good quality homogeneous particles, mostly in spherical shape are observed. In case of higher concentration of Yb^{3+} ions the irregular clusters of grains without visible grain boundaries covered by a second phase in the form of cube-shaped crystals are present. This second phase is corresponding to the monoclinic stoichiometric Yb_2MoO_6 phase. The low temperature emission spectra of Yb^{3+} probe ions-doped $La_2Mo_2O_9$ show three components of 0-phonon line for monoclinic molybdates and broad but not resolved 0-phonon line for cubic molybdates. Both results indicate the multisite character of Yb^{3+} ions in each of main un-equivalent sites of the $La_2Mo_2O_9$ structure which are consistent with research performed for Yb^{3+}-doped mixed La_2MoWO_9. Consequently, it can be assumed that the environment of all Yb^{3+} ions can be distinguished as, first of all, two types of polyhedra YbO_7 and YbO_8 like in Yb^{3+}-doped La_2MoWO_9 and secondly by a third type of YbO_9 polyhedron. Our results are confirmed by the decay time measurements. Summing up the results, it is evident strongly influence of the concentration of Yb^{3+} ions and type of crystallographic system on the luminescence properties.

In view of continuous research on application of the cubic molybdates or tungstates as cubic laser ceramics, the new Yb^{3+}-doped $La_2Mo_2O_9$ are less promising candidates in contrast to the Yb^{3+}-doped mixed La_2MoWO_9, which stabilize the pure cubic system in a whole concentration range (0.1–20 mol%). Also all the samples are very homogeneous.

We have shown that Yb^{3+} rare earth is a probe ion. It gives a new deeper contribution of the complex structure of both La_2MoO_9 and La_2MoWO_9 molybdate families. Our approach is similar with the analysis we have previously done with Nd^{3+} ion, which can be also used as a structural probe one. More generally we should bring all contributions to the knowledge of these crystallographic structures from the spectroscopic properties of rare earth optical ions. In this way, the spectroscopy of Eu^{3+} rare earth probe ion should bring complementary results in the next step.

First translucent ceramics of 3 mol% Yb^{3+}-doped $La_2Mo_2O_9$ and 3 mol% Yb^{3+}-doped La_2MoWO_9 ceramics have been successfully fabricated. The comparison turns out in favor of Yb^{3+}-doped mixed La_2MoWO_9. The structural and spectroscopic differences are also significant for these materials. SEM images with the EDS elemental analysis show for both cases inhomogeneous morphology consisted of quite large grains with circular shape and much smaller, white points mostly accumulated at the grain boundaries which contain higher amount of Yb^{3+} ions than at the grains surface. So, in both cases we deal with phase segregation in first translucent ceramics.

17.3.2 Yb^{3+}-Doped Y_6MoO_{12}

17.3.2.1 Structure Characterization

Basing on the article of Fournier [64] from 1970 devoted to deep research on Ln_2O_3-MoO_3 systems and Ln_6MoO_{12} phases, we know that Y_6MoO_{12} ($3Y_2O_3$:MoO_3) can exist in two forms: until 1480 °C – low temperature orthorombic phase and above 1500 °C – high temperature face cantered, cubic (Z = 4) structure, which is very stable. The compositions with chemical formula Ln_6MoO_{12} previously investigated by Aikten [65] and Bartram [66] were attributed to the cubic and orthorhombic structures. Fournier et al. have repeated the investigations by preparing the samples at 1350 °C, excepting the Y_6MoO_{12} and Er_6MoO_{12} obtained at 1500 °C. Thanks to this research which we know that stoichiometric molybdates with La, Pr, Nd, Sm, Eu, Gd, Tb, Dy and Ho crystallize in the cubic phase already at 1350 °C [64]. The three last lanthanides *i.e.* Tm, Yb and Lu do not give the cubic Ln_6MoO_{12} phase event at 1525 °C. Maybe this transformation could be possible at much higher temperature. It is necessary to add that all information on the structure of Ln_6MoO_{12} described by Fournier based on the refinements of XRD powder patterns and in the literature there is no information of crystal structure from the single crystals of Y_6MoO_{12}. This is why it is a great need to obtain samples in the form of single crystals.

Nevertheless, the crystal structure of Y_6WO_{12} crystalized in the rhombohedral system (S.G. R3 and Z = 3 for the R-centered setting) from the Rietveid refinement reported by Diot [67] can be helpful to discussion of Y_6MoO_{12} structure. Obtained at 1300 °C/24 h ternary oxides of Y_6WO_{12} crystallize with a three-dimensional

rhombohedral structure closely related to that of the binary oxides Ln_7O_{12} and deriving from the ideal fluorite structure. In this case the yttrium ion is sevenfold coordinated with Y-O bond length ranging from 2.19 to 2.70 Å. The coordination polyhedron may be described as a mono-capped trigonal prism. The tungsten atom is located at the center of a WO_6 octahedron with unique W-O distances of 1.98 and 1.92 Å. In the crystal structure of Y_6WO_{12}, W atoms occupy 3a (0, 0, 0) octahedral sites with six O atoms around them, forming slightly deformed WO_6 octahedra, while Y atoms occupy 18f (x, y, z) sites and they are coordinated to three O1 atoms and four O2 atoms, having C_1 point symmetry. The WO_6 and YO_7 polyhedra are connected each other by sharing corners and edges [67]. It is important to notice that at the temperature 1200 °C/12 h the Y_6WO_{12} represents the hexagonal system. According to the literature, [66, 68, 69] Y and Mo ions be distributed randomly in the cationic sublattice, and O ions and O vacancies should be distributed randomly in the anionic sublattice. An ordered distribution of Mo and O vacancies will result in a related hexagonal phase. For the isostructural Y_6WO_{12}, the disordered cubic fluorite phase is considered to be metastable. As regard to Y_6MoO_{12}, a coexistence of cubic and hexagonal phases was obtained from solid-state reaction, while the only cubic phase was observed from the chemical solution method [54]. This indicates that the stability of the cubic phase is equivalent or surpassing that of the hexagonal phase.

The Yb^{3+}-doped Y_6MoO_{12} micro-powders were characterized by XRD method to verify the phase purity. Figure 17.17 plots experimental results as a function of the Yb^{3+} concentration compared with the simulated XRD pattern of cubic Y_6MoO_{12} (ICSD#30-1456) from the database of inorganic crystal structures [31]. It is obvious that all the diffraction peaks of these samples are in good agreement with the pure Y_6MoO_{12} and no other phases as impurities can be detected. This result indicates that the Yb^{3+} ions were completely incorporated into the Y_6MoO_{12} host lattice without making significant changes to the crystal structure. As the ionic radius of Yb^{3+} ($r = 0.925$ Å, $CN = 7$) is smaller that of Y^{3+} ($r = 0.96$ Å, $CN = 7$), we suppose that Yb^{3+} ions occupy Y^{3+} sites. The un-doped and Yb^{3+}-doped Y_6MoO_{12} crystallize as disordered cubic fluorite phase with a space group of Fm-3 m and the lattice constants are calculated to be $a = 5.29$ Å. From literature we know also that the fluorite structure is capable to construct superstructures with its flexible nature [29, 31].

The lattice parameter calculated basing on the indexing powder diffraction patterns were reported recently [49]. The substitution of Y^{3+} ions by smaller Yb^{3+} leads to systematic decrease in the lattice parameters, thus we observed linear dependence of lattice constant vs. Yb^{3+} content for cubic Yb^{3+}-doped Y_6MoO_{12}. Furthermore, using the pycnometric method, an experimental density of each obtained solution was determined. The unit cell parameter and the volume calculated for each analyzed solution satisfy the Vegard law [49].

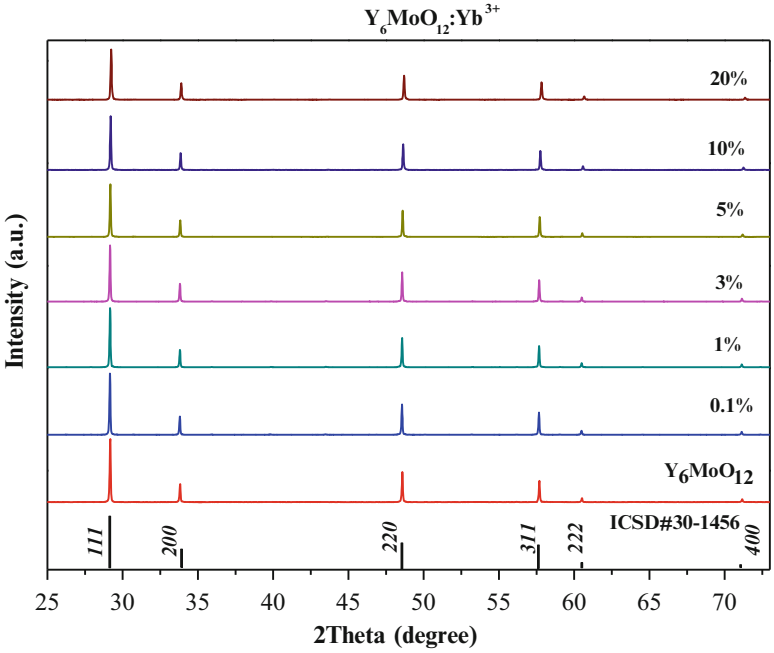

Fig. 17.17 X-ray powder diffraction patterns of Y_6MoO_{12} and Yb^{3+}-doped Y_6MoO_{12} solid solutions with different contents of the Yb^{3+} optically active ions

17.3.2.2 Morphology and Particle Size by SEM

According to very high sintering temperatures (1550 °C) applied in the solid-state reaction to obtain pure cubic phase the grains formed micro-crystallites with a grain size in the range from 0.5 to even 8 μm. A large impact on the size has also the fact that the reactions do not occur quickly and violently as in the case of the combustion method.

As an example in Fig. 17.18 we present the SEM (Scanning Electron Microscope) micrographs Y_6MoO_{12} compound and Yb^{3+}-doped Y_6MoO_{12} solid solutions with a different content of the active ion. The overview pictures show a good quality materials. Aggregates composed of grains and a type of boundary between the microcrystals of powders with different concentrations of Yb^{3+} ions can be seen. The overview pictures show separated particles and loose clusters. However, they create also the bigger forms by aggregation of the smaller grains of irregular forms. For Yb^{3+}-doped Y_6MoO_{12} solid solutions no second phase formation was observed, the samples are very homogeneous.

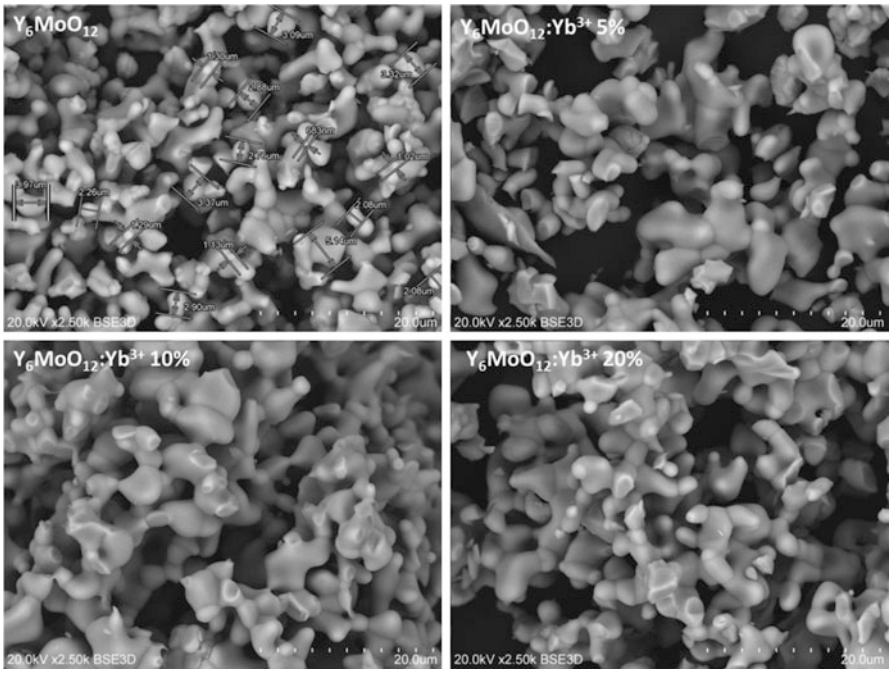

Fig. 17.18 SEM micrographs of Y_6MoO_{12} and Yb^{3+}-doped Y_6MoO_{12} solid solutions

17.3.2.3 Absorption Spectra

The relative energy of the Yb^{3+} Stark levels was investigated by optical absorption (4.2 K) and photoluminescence (77 K) measurements in near infrared region (NIR). Fig. 17.19 presents the absorption spectra for 20 mol% Yb^{3+} in Y_6MoO_{12} recorded at room and liquid helium temperatures. At RT the spectra consist of broad weakly resolved bands located between 850 nm and 1100 nm corresponding to the transition from the $^2F_{7/2}$ ground state of Yb^{3+} to the three Stark components of the $^2F_{5/2}$ excited state. The absorption line relates to the so-called zero phonon line, from the lowest Stark component to the $^2F_{7/2}$ (1) ground state to the lowest Stark level of the $^2F_{5/2}$ (5) is located at around 976 nm and it is the strongest absorption line. The others lines corresponding to the $^2F_{7/2}$ (1) → $^2F_{5/2}$ (6) and to $^2F_{7/2}$ (1) → $^2F_{5/2}$ (7) transitions are at room temperature not very well formed. Going to the low temperature we are able to distinguish four components located at 875, 905, 920 and 949 nm, respectively. We supposed that the bands of highest intensities at 920 and 949 nm originated from (1) → $^2F_{5/2}$ (7) and $^2F_{7/2}$ (1) → $^2F_{5/2}$ (6) transitions respectively and those at 875 and 905 nm might possess the vibronic character, the same as the line of small intensity at 963 nm.

The measurements performed at 4.2 K should lead to narrowing and better resolution of the main electronic Stark components, however it is not case for

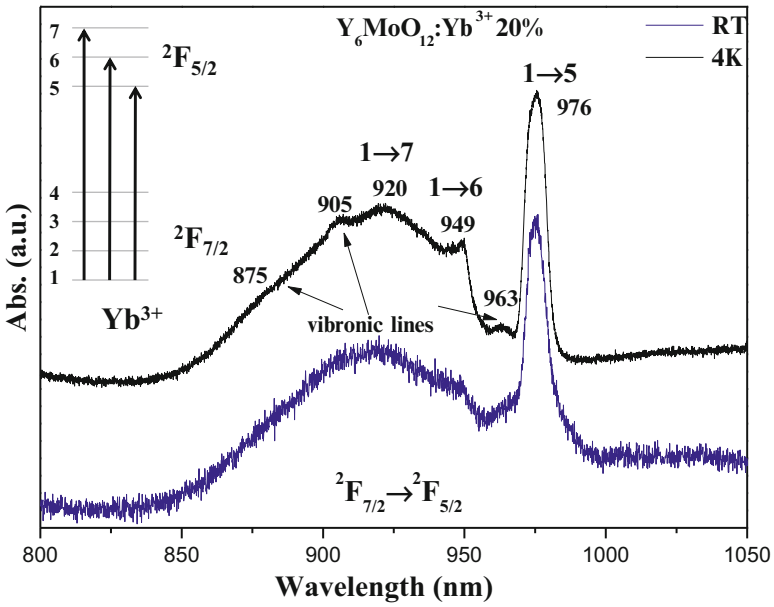

Fig. 17.19 Absorption spectra of Yb^{3+}-doped Y_6MoO_{12} solid solution recorded at room and liquid helium temperatures

Y_6MoO_{12} host lattice. As the ionic radius of Yb^{3+} (r = 0.925 Å, CN = 7) is slightly smaller that of Y^{3+} (r = 0.96 Å, CN = 7), we supposed that the Yb^{3+} ions introduced to the network occupy the Y^{3+} site. There is not a very large difference in the ionic radii, so that the disorder in the structure will not be significant. It will be at least smaller than in case when we substitute the La^{3+} ion (r = 1.1 Å, CN = 7) by the Yb^{3+} one [47].

According to the crystal-field theory of Kramer's ions, the maximum of allowed components splitting for J = 5/2 state is three; therefore, for one symmetry site the absorption spectrum at liquid helium temperature should be resolved into three bands. The 0-phonon line is a sharp one and contains only one component at 4.2 K. The total splitting of the excited $^2F_{5/2}$ state 624 cm^{-1} is similar like that observed for some other matrices like sesquioxides (about 793 cm^{-1}) [70], $K_5Bi(MoO_4)_4$ molybdates [71] orthohosphates (750–800 cm^{-1}) [72] but much larger than we reported recently for La_2MoWO_9 474 cm^{-1} [47] and 454 cm^{-1} for $CdMoO_4$ [26]. The interest of high splitting is clear for solid state lasers with a near 4-levels scheme.

17.3.2.4 Concentration Dependence and Excitation Wavelength Dependences of the Photoluminescence Spectra

The emission spectra of Y_6MoO_{12} activated with different concentrations of Yb^{3+} ion registered at room temperature under λ_{ex} = 915 nm of a Ti- Sapphire laser are

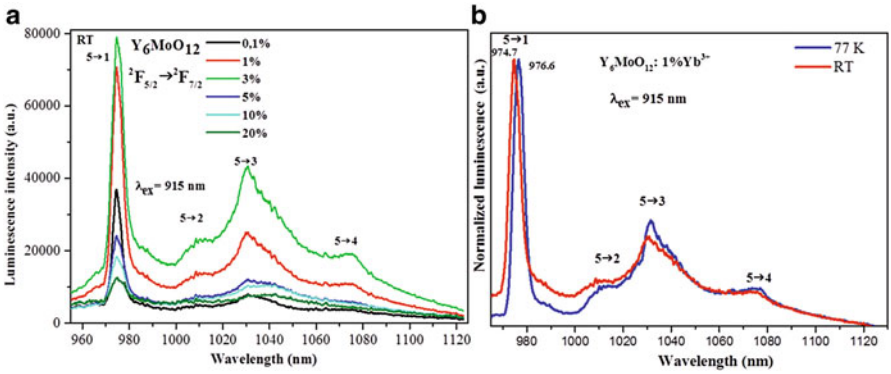

Fig. 17.20 Room temperature (RT) emission spectra of Yb^{3+}-doped Y_6MoO_{12} solid solutions with different concentrations of Yb^{3+} activator

plotted in Fig. 17.20a. The studied materials exhibit the usual luminescence lines in the near-infrared region from the $^2F_{5/2} \rightarrow {}^2F_{7/2}$ transitions of Yb^{3+} ions. At RT the lines are broad, however it is possible to distinguish the four components corresponding to the transitions from the lowest Stark level of the $^2F_{5/2}$ excited state (5) to each of the four Stark levels of the $^2F_{7/2}$ state (1, 2, 3, 4), respectively.

The (5 → 1) component is located at around 975–977 nm. In case of Y_6MoO_{12} solid solutions we can distinguish the lines at 974.7 nm (5 → 1), 1010 nm (5 → 2), 1030 nm (5 → 3) and 1075 nm (5 → 4). Starting from 5 mol% up to 20 mol% one can distinguish a second component of the 0-phonon (5 → 1) line located at 977 nm indicating a second type of Yb^{3+} site in this matrix. The maximum concentration of Yb^{3+} ions in this host lattice where the luminescence intensity is the highest was set at 3 mol%. For this sample, and also for 1 mol%, we can observe also very low components at 965 nm and 987 nm, which may correspond to vibronic transitions. Going to the 4.2 K the shape of the emission spectra stay the same although we should observe the narrowing of the lines. Very slight narrowing of the lines was also observed in the absorption spectra presented in the previous paragraph indicating some disorder degree of the active ions in the host. A clear change observed in the emission spectra of low Yb^{3+} concentration (1%) with decreasing temperature is the shifting of the 0-phonon line from 974.7 nm at RT to 976.6 nm at 4.2 K (see Fig. 17.20b). The multisite distribution of Yb^{3+} ions in Y_6MoO_{12} solid solution as a probe of some disorder can be seen by the temperature dependence of both, the unusual slight shift of the 0-phonon line in luminescence spectra, and almost the same half-widths at half maximum (FWHM) of this 0-phonon line (54 cm^{-1} at 77 K and 59 cm^{-1} at RT). Low temperature emission spectra recorded under site selective excitation of Ti-sapphire laser are presented in Fig. 17.21 for 1% Yb^{3+}. The spectra are normalized to show the differences in the shape of lines under different excitation wavelength. Nevertheless, we have performed also the comparison of the luminescence intensity of all samples by recording the spectra under the same conditions. The highest intensity has been observed for 5 → 3

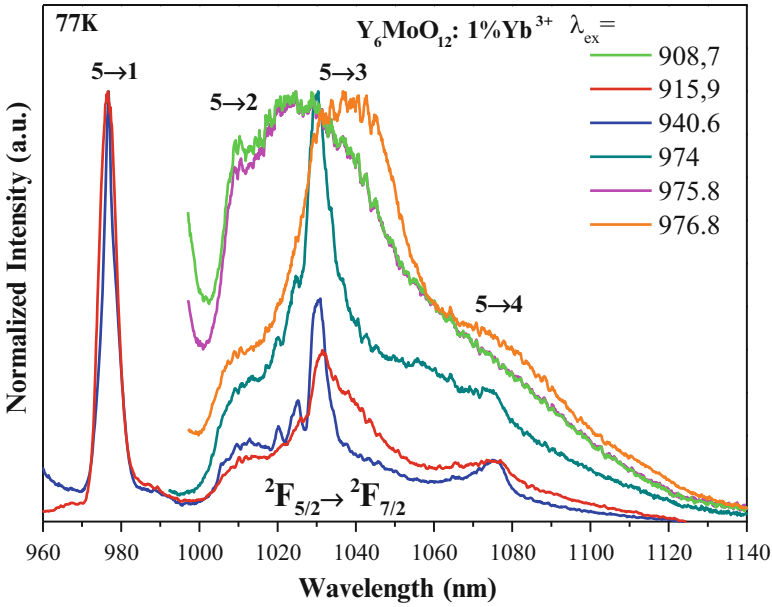

Fig. 17.21 Low temperature emission spectra of 1 mol% Yb^{3+}-doped Y_6MoO_{12} solid solution under site selective excitations of Ti-sapphire laser

transition at 1030 nm (the laser line when materials are used as laser source) under 974 nm pumping. It is between 2.8 times and 7 times more higher than for any other excitation lines of the tunable Ti-sapphire. The position of zero-phonon line from the absorption spectra stay in good agreement with that from the emission. Under the excitation of 915.9 nm four lines are clearly resolved. The main lines corresponding to the four Stark emission components are located at 976 nm (5 → 1), 1010 nm (5 → 2), 1030 nm (5 → 3) and 1075 nm (5 → 4), respectively. Under excitation at 940.6 nm the additional weak components at 1020 nm and 1025 nm is the result of electron– phonon coupling with M–O modes. When the excitation wavelength changes we can especially observe the shifting of the 5 → 3 transition to higher energy wavelengths i.e. at 1025 nm for excitation 908.7 nm and 975.8 nm or to infrared region (1037 nm) for excitation at 976.8 nm confirming the distribution of Yb^{3+} ions in, at least, three non- equivalent sites in the lattice. In addition, these bands start to be broad and the shifting from 1025 nm to 1037 nm is a result of changing the excitation line of only of 1 nm. We suppose in the case of Y_6MoO_{12} we observe the main distribution of Yb^{3+} ions under excitation at 915.9, 940.6 and 974 nm respectively, giving the highest intensity of the usual laser line at 1030 nm. We obtain similar well resolved spectra and two slightly distorted symmetry sites of Yb^{3+} ions for other excitations yielding the shifted lines observed at 1025 and 1037 nm.

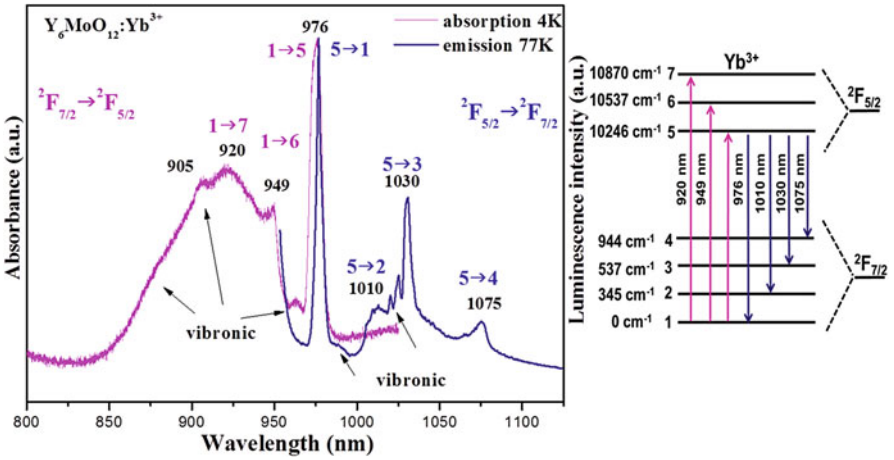

Fig. 17.22 Absorption and emission spectra at low temperatures and Stark splitting levels of Yb^{3+} ion

17.3.2.5 Yb^{3+} Energy Level Diagram in Y_6MoO_{12}

Figure 17.22 presents the low temperature absorption and emission spectra of 10 mol% Yb^{3+}-doped Y_6MoO_{12} which allowed to propose the drawn energy level scheme of Yb^{3+} ion in this matrix. An energy level diagram can be derived from low temperature measurements. The splitting both of ground state as well as the excited state is quite large if we compare with other cubic matrix recently reported by us *i.e.* Yb^{3+}-doped La_2MoWO_9.

17.3.2.6 Decay Analysis

The decay curves of x% Yb^{3+}-doped Y_6MoO_{12} solid solutions (x-0.1-50) were obtained under laser pulsed excitation at 940 nm (some of them at 980 nm) in the $^2F_{7/2}$ (1) → $^2F_{5/2}$ (6) absorption line and by monitoring 1030 nm $^2F_{5/2}$ (5) → $^2F_{7/2}$(2) emission. Table 17.2 summaries the decay times for Yb^{3+}-doped Y_6MoO_{12} with different concentration of Yb^{3+} ions recorded at room and low temperatures. The decays curves (not shown here) are exponential at low temperature for most of samples while at room temperature only for the lowest concentration (0.1 mol%) the decay curve keep the exponential shape with a fitted lifetime of about 285 μs at room temperature and 340 μs 77 K corresponding to the radiative lifetime. For the concentration of 3 and 5% energy transfer occurs between centers. Then, for the concentration above 10% self-quenching phenomena is predominant. When we compare Yb^{3+}-doped Y_6MoO_{12} solid solutions with another cubic composition evaluated recently by us as Yb^{3+}-doped La_2MoWO_9 and also with tetragonal Yb^{3+}-doped $CdMoO_4$ solid solution, we clearly see the difference [47, 73] concerning

Table 17.2 Luminescence decays times of cubic Yb^{3+}-doped Y_6MoO_{12} solid solutions recorded at room temperature and 77 K, $\lambda_{ex} = 940$ nm (some of them at 980 nm) and $\lambda_{em} = 1030$ nm

	0.1%	1%	3%	5%	10%	20%	50%
RT (μs)	285	250	128	45	17	6.5	1.5
77 K (μs)	340	340	275	112	32	11	2

the usual self-trapping process which is not observed in this matrix. Only the self-quenching process appears here. For investigated previously micro-crystallites, also obtained by the high temperature solid state method, with similar grain sizes the transfer of energy between the Yb^{3+} ions i.e. self-trapping process was easily observed due to short distances between Yb^{3+} ions where resonant diffusion occurs (3.66 Å in $CdMoO_4$ and 3.15 Å in La_2MoWO_9). It means that in Yb^{3+}-doped Y_6MoO_{12} the unknown distance between Yb^{3+} ions should be much higher than these values to reduce this process.

17.3.2.7 Conclusion on Yb^{3+}-Doped Y_6MoO_{12} Cubic Material

Other investigated group is Yb^{3+}-doped Y_6MoO_{12} solid solutions crystallizing as disordered cubic fluorite phase with a space group of Fm-3 m and the calculated lattice constants 5.29 Å. This material is thermally stable up to 1500 °C. All micro-powders obtained by high-temperature solid state reaction possess the yellow colour. The SEM images showed relatively big grains with the average size of few micrometers (0.5–8 μm) due to the high temperature (1550 °C) of synthesis. All the samples are very homogenous without other phase segregation and no significant change of the grain size with changing the activator concentration is observed. Relatively broad absorption lines in NIR region suggest disordering of the active ions in the structure. This phenomena is smaller than for cubic Yb^{3+}-doped La_2MoWO_9 molybdato-tungstates, what is a consequence of the smallest difference of ionic radii between Yb^{3+} (0.925 Å, CN = 7) and Y^{3+} (0.96 Å) ions in Yb^{3+}-doped Y_6MoO_{12} than between Yb^{3+} (0.925 Å) and La^{3+} (1.1 Å) ions in Yb^{3+}-doped La_2MoWO_9. Well formed in low temperature absorption spectra electronic transitions point out only one symmetry site in Yb^{3+}-doped Y_6MoO_{12}, but we observe also many vibronic components, what make very difficult the interpretation of the spectra. The NIR emission spectra recorded at RT are characterized by broad lines, and it is possible to distinguish four components corresponding to the transitions from the lowest Stark level of the $2F_{5/2}$ excited state (5) to each of the four Stark levels of the $^2F_{7/2}$ state (1, 2, 3, 4), respectively. Also in this case the band are assisted by the vibronic transitions. Very slight narrowing of the emission lines like in the absorption spectra is indicating a disorder of the active ions in the host. The multisite character in Yb^{3+}-doped $Y6MoO_{12}$ has been confirmed by the shifting of the 0-phonon line from 974.7 nm at RT to 976.6 nm at 4.2 K under the same excitation at 915 nm. Another evidence for the multisite character can be found in the site selective excitation spectra, where

change of excitation lines results in three different spectra. Thus, we observe three types of Yb^{3+} site symmetry, one main distribution of Yb^{3+} ions and two slightly distorted sites. Basing on the low temperature absorption and emission energy level diagram has been proposed. When we compare with other cubic matrix recently reported by us, i.e. Yb^{3+}-doped La_2MoWO_9, one can notice the advantage of the largest splitting both of the $^2F_{7/2}$ ground state as well as the $^2F_{5/2}$ excited one with Y_6MoO_{12} molybdate what is an important property in laser materials. The decays curves are exponential at low temperature for most of samples while at room temperature only for the lowest concentration (0.1 mol%) the decay curve keep the exponential shape with a fitted lifetime of about 285 μs and 340 μs 77 K corresponding to the radiative lifetime. When the concentration of Yb^{3+} ions increases the usual energy transfer occurs between centers so that the self-quenching phenomena is predominant. We didn't observe any self-trapping effect in this matrix meaning higher distances between Yb^{3+}- Yb^{3+}) ions than in cubic Yb^{3+} – doped La_2MoWO_9 and tetragonal Yb^{3+}-doped $CdMoO_4$ previously analyzed by us.

Concluding, the first studies have shown many advantages of this material and in the step of our program we will prepare the nano-powdered samples to succeed the fabrication in the form of transparent optical ceramics.

17.4 General Conclusion

A purpose of the paper is to summarize the first results obtained for Yb^{3+}-doped molybdates and molybdato-tungstates synthesized by the high-temperature solid-state reaction and crystallizing in the cubic system: $La_2Mo_2O_9$ /La_2MoWO_9 /Y_6MoO_{12} for future new transparent optical ceramics. We investigate the correlation between structural and spectroscopic properties of mentioned above compositions. Yb^{3+} rare earth dopant has been used as a structural probe in addition of the intrinsic interest to be a laser ion.

This probe ion gives a new deeper contribution of the complex structure of both La_2MoO_9, La_2MoWO_9 and Y_6MoO_{12} molybdate families. Our approach is similar with the analysis we have previously done with Nd^{3+} laser ion, which can be also used as a structural probe one. More generally we should bring all contributions to the knowledge of these crystallographic structures from the spectroscopic properties of rare earth optical ions. In this way, the spectroscopy of Eu^{3+} rare earth probe ion should bring complementary results in the next step.

The first studies of Yb^{3+}-doped Y_6MoO_{12} have shown many advantages of this material and in the step of our program we will prepare the nano-powdered samples to succeed the fabrication in the form of transparent optical ceramics.

The research is under progress to get high quality optical transparent ceramics from the technique of sintering nano-crystalline powders by using both the fast SPS (Spark Plasma Sintering) and known HIP (Hot Isostatic Pressing) techniques.

Acknowledgements The authors would like to thank for the financial support from National Science Center of Poland for the grant HARMONIA 8 No UMO-2016/22/M/ST5/00546 and also the Minister of Science and Higher Education in Poland and in France for the Grant POLONIUM for scientific exchange between Institute Light Matter (ILM), University Claude Bernard Lyon1, in France and Faculty of Chemistry, University of Wroclaw in Poland. Moreover, the financial support from the French Embassy in Warsaw (French Government scholarship for research stage for M. Guzik in Lyon) is gratefully acknowledge.

References

1. Dey S, Ricciardo RA, Cuthbert HL, Woodward PM (2014) Metal-to-metal charge transfer in AWO_4 (A = Mg, Mn, Co, Ni, Cu, or Zn) compounds with the wolframite structure. Inorg Chem 53:4394–4399
2. Feldmann C, Justel T, Ronda CR, Schmidt PJ (2003) Inorganic luminescent materials: 100 years of research and application. Adv Funct Mater 13:511–516
3. Brixner LH (1987) New X-ray phosphors. Mater Chem Phys 16:253–281
4. Mikhailik VB, Kraus H, Miller G, Mykhaylyk MS, Wahl D (2005) Luminescence of $CaWO_4$, $CaMoO_4$, and $ZnWO_4$ scintillating crystals under different excitations. J Appl Phys 97:083523
5. Mikhailik VB, Kraus H, Kapustyanyk V, Panasyuk M, Prots Y, Tsybulskyi V, Vasylechko L (2008) Structure, luminescence and scintillation properties of the $MgWO_4$-$MgMoO_4$ system. J Phys Condens Matter 20:365219
6. Kobayashi M, Ishii M, Harada K, Usiki Y, Okuno H, Shimizu H, Yazawa T (1996) Scintillation and phosphorescence of $PbWO_4$ crystals. Nucl Instrum Method Phys Res Sect A 373:333–346
7. Kaminskii A, McCray CL, Lee HR, Lee SW, Temple DA, Chyba TH, Marsh WD, Barnes JC, Annanenkov AN, Legun VD et al (2000) High efficiency nanosecond Raman lasers based on tetragonal $PbWO_4$ crystals. Opt Commun 183:277–287
8. Nikl M, Nitsch K, Polak K, Mihokova E, Dafinei I, Auffray E, Lecoq P, Reiche P, Uecker R, Pazzi GP et al (1996) Slow components in the photoluminescence and scintillation decays of $PbWO_4$ single crystals. Phys Status Solidi B 195:311–323
9. Pujol MC, Mateos X, Sole R, Massons J, Gavalda J, Solans X, Dias F, Aguilo M (2002) Structure, crystal growth and physical anisotropy of $KYb(WO_4)_2$, a new laser matrix. J Appl Crystallogr 35:108–112
10. Boulon G, Metrat G, Muhlstein N, Brenier A, Kokta MR, Kravchik L, Kalisky Y (2003) Efficient diode-pumped Nd:$KGd(WO_4)_2$ laser grown by top nucleated floating crystal method. Opt Mater 24:377–383
11. Brenier A, Bourgeois F, Metrat G, Muhlstein N, Boulon G (2001) Spectroscopic properties at 1.351 μm of Nd^{3+}-doped $KY(WO_4)_2$ and $KGd(WO_4)_2$ single crystals for Raman conversion. Opt Mater 16:207–211
12. Kaminskii AA (1981) Laser crystals: their physics and properties. Springer, Berlin/Heidelberg/New York
13. Feng X, Feng W, Xia M, Wang K, Liu H, Deng D, Qin X, Yao W, Zhu W (2016) Co-precipitation synthesis, photoluminescence properties and theoretical calculations of $MgWO_4$:Eu^{3+} phosphors. RSC Adv 6:14826–14831
14. Zhang WJ, Feng WL, Nie YM (2015) Photoluminescence properties of red europium doped calciumtungstate phosphors for blue-pumped light-emitting diodes. Optik 126:1341–1343
15. Feng WL, Tao CY, Wang K (2015) Synthesis and photoluminescence of tetravalent cerium-doped alkaline-earth-metal tungstate phosphors by a co-precipitation method. Spectrosc Lett 48:381–385
16. Itoh M (2012) Luminescence study of self-trapped excitons in $CdMoO_4$. J Lumin 132: 645–651

17. Sczancoski JC, Bomio MDR, Cavalcante LS, Joya MR, Pizani PS, Varela JA, Longo E, Li S, Andrés JA (2009) Morphology and blue photoluminescence emission of $PbMoO_4$ processed in conventional hydrothermal. J Phys Chem C 113:5812–5822
18. Minowa M, Itakura K, Moriyama S, Ootani W (1992) Measurement of the property of cooled lead molybdate as a scintillator. Nucl Instrum Method Phys Res Sect A 320:500–503
19. Hizhnyi YA, Nedilko SG (2003) Investigation of the luminescent properties of pure and defect lead tungstate crystals by electronic structure calculations. J Lumin 102−103:688–693
20. Kudo A, Steinberg MA, Bard J, Campion A, Fox MF, Mallouk TE, Webber SE, White JM (1990) Photoactivity of ternary lead-group VIB oxides for hydrogen and oxygen evolution. Catal Lett 5:61–66
21. Sczancoski JC, Cavalcante LS, Joya MR, Varela JA, Pizani PS, Longo E (2008) $SrMoO_4$ powders processed in microwave- hydrothermal: synthesis, characterization and optical properties. Chem Eng J 140:632–637
22. Sczancoski JC, Cavalcante LS, Marana NL, da Silva RO, Tranquilin RL, Joya MR, Pizani PS, Varela JA, Sambrano JR, Siu L et al (2010) Electronic structure and optical properties of $BaMoO_4$ powders. Curr Appl Phys 10:614–624
23. Thongtem T, Kungwankunakorn S, Kuntalue B, Phuruangrat A, Thongtem S (2010) Luminescence and absorbance of highly crystalline $CaMoO_4$, $SrMoO_4$, $CaWO_4$ and $SrWO_4$ nanoparticles synthesized by co-precipitation method at room temperature. J Alloys Compd 506:475–481
24. Feng W, Lin H, Liu H (2015) Photoluminescence and crystal-field analysis of Pr^{3+}-doped $SrMoO_4$ phosphors. Z Naturforsch 70(1a):11–16
25. Guzik M, Tomaszewicz E, Guyot Y, Legendziewicz J, Boulon G (2015) Structural and spectroscopic characterizations of new $Cd_{1-3x}Nd_{2x}€_xMoO_4$ scheelite-type molybdates with vacancies as potential optical materials. J Mater Chem C 3:40574069
26. Guzik M, Tomaszewicz E, Guyot Y, Legendziewicz J, Boulon G (2016) Spectroscopic properties, concentration quenching and Yb^{3+} site occupations in vacancied scheelite-type molybdates. J Lumin 169:755–764
27. Guzik M, Tomaszewicz E, Guyot Y, Legendziewicz J, Boulon G (2015) Eu^{3+} luminescence from different sites in a scheelite- type cadmium molybdate red phosphor with vacancies. J Mater Chem C 3:8582–8594
28. Boulon G (2012) Fifty years of advances in solid-state laser materials. Opt Mater 34:499–512
29. Sanghera J et al (2011) Transparent ceramics for high-energy laser systems. Opt Mater 33: 511–518
30. Sanghera J, Kim W, Villalobos G, Shaw B, Baker C, Frantz J, Sadowski B, Aggarwal I (2013) Ceramic laser materials: past and present. Opt Mater 35:693–699
31. Ikesue A, Aung YL (2008) Ceramic laser materials. Nat Photonics 2:721–727
32. Ikesue A, Kinoshita T, Kamata K, Yoshida K (1995) Fabrication and optical properties of high-performance polycrystalline Nd:YAG ceramics for solid-state lasers. J Am Ceram Soc 78(4):1033–1040
33. Heller A (2006) Transparent ceramics spark laser advances. Sci Technol Rev:10−17
34. Bishop A (2009) Northrop Grumman scales new heights in electric laser power, achieves 100 kW from a solid-state laser. Globe Newswire 18
35. Takaichi K, Yagi H, Lu J, Shirakawa A, Ueda K, Yanagitani T, Kaminskii AA (2003) Yb^{3+}-doped $Y_3Al_5O_{12}$ ceramics – a new solid-state laser material. Phys Status Solidi 200(1):R5–R7
36. Esposito L, Epicier T, Serantoni M, Piancastelli A, Alderighi D, Pirri A, Toci G, Vannini M, Anghel S, Boulon G (2012) Integrated analysis of non-linear loss mechanisms in Yb:YAG ceramics for laser applications. J Am Ceram Soc 32(10):2273–2281
37. Lu J et al (2002) Promising ceramic laser material: highly transparent Nd^{3+}:Lu_2O_3 ceramic. Appl Phys Lett 81:4324–4326
38. Sanghera J, Kim W, Baker C, Villalobos G, Frantz J, Shaw B, Lutz A, Sadowski B, Miklos R, Hunt J, et al. (2011) Laser oscillation in hot pressed 10% Yb^{3+}:Lu_2O_3 ceramic. Opt Mater 33(5):670–674

39. An L, Ito A, Zhang J, Tang D, Goto T (2014) Highly transparent Nd^{3+}:Lu_2O_3 produced by spark plasma sintering and its laser oscillation. Opt Mater Exp 4(7):1420–1426
40. Toci G et al (2015) Nd^{3+}-doped Lu_2O_3 transparent sesquioxide ceramics elaborated by the spark plasma sintering (SPS) method. Part 2: First laser output results and comparison with Nd^{3+}-doped Lu_2O_3 and Nd^{3+}-Y_2O_3 ceramics elaborated by a conventional method. Opt Mater 41:12–16
41. Li W, Mei B, Song J (2015) Nd^{3+}, Yb^{3+}-codoped SrF_2 laser ceramics. Opt Mater 47:108–111
42. Georges S, Goutenoire F, Altorfer F, Sheptyakov D, Fauth F, Suard E, Lacorre P (2003) Thermal, structural and transport properties of the fast oxide-ion conductors La-xRxMo2O9 (R=Nd,Gd,Y). Solid State Ionics 161:231–241
43. Kuang W, Fan Y, Yao K, Chen YJ (1998) Preparation and characterization of ultrafine rare earth molybdeum complex oxide particles. J Solid State Chem 140:354–360
44. Guzik M, Bieza M, Tomaszewicz E, Guyot Y, Boulon G (2014) Development of Nd^{3+}-doped monoclinic dimolybdates $La_2Mo_2O_9$ as optical materials. Z Naturforsch 69b:193–204
45. Guzik M, Bieza M, Tomaszewicz E, Guyot Y, Zych E, Boulon G (2015) Nd^{3+} dopant influence on the structural and spectroscopic properties of microcrystalline $La_2Mo_2O_9$ molybdate. Opt Mater 41:21–31
46. Bieza M, Guzik M, Tomaszewicz E, Guyot Y, Lebbou K, Zych E, Boulon G (2017) Toward optical ceramics based on cubic Yb^{3+} rare earth ion-doped mixed molybdato-tungstates: Part I – Structural characterization. J Phys Chem C 121:13290–13302
47. Bieza M, Guzik M, Tomaszewicz E, Guyot Y, Boulon G (2017) Toward optical ceramics based on Yb^{3+} rare earth ion-doped mixed molybdato-tungstates: Part II – Spectroscopic characterization. J Phys Chem C 121:13303–13313
48. Bieza M, Guzik M, Tomaszewicz E, Guyot Y, Boulon G (2017) Yb^{3+} rare earth structural probe and correlation between morphology and spectroscopic properties in $La_2Mo_2O_9$. Comparative analysis with mixed cubic La_2MoWO_9 translucent ceramics. J Eur Ceram Soc 38:3217–3234
49. Bieza M, Guzik M, Tomaszewicz E, Guyot Y, Boulon G (2017) Cubic Yb^{3+}-activated Y_6MoO_{12} micro-powder e optical material operating in NIR region. Opt Mater 63:3–12
50. Zhao X, Zhang Y, Huang Y, Gong H, Zhao J (2015) Synthesis and characterization of neodymium doped yttrium molybdate high NIR reflective nano pigments. Dyes Pigments 116:119–123
51. Zhang X, Zhang Y, Gong H, Zhao X, Wang C, Zhu H (2013) Synthesis, characterization and optical properties of $Y_{6-x}Sm_xMoO_{12+\sigma}$ composite/compounds pigments with high near-infrared reflectance. Adv Mater Res 602–604:102–106
52. George G, Vishnu VS, Reddy MLP (2011) 6. The synthesis, characterization and optical properties of silicon and praseodymium doped Y_6MoO_{12} compounds: Environmentally benign inorganic pigments with high NIR reflectance. Dyes Pigments 88:109–115
53. Li H, Pu X, Yin J, Wang X, Yao NSM, Jeong JH (2016) Effect of crystallite size and crystallinity on photoluminescence properties and energy transfer of Y_6MoO_{12}:Eu. J Am Ceram Soc 99(3):954–961
54. Li H, Yang HK, Moon BK, Choi BC, Jeong JH, Jang K, Lee HS, Yi SS (2011) Investigation of the structure and photoluminescence properties of Eu^{3+} ion-activated $Y_6W_xMo_{(1-x)}O_{12}$. J Mater Chem 21:4531–4537
55. Li H, Noh HM, Moon BK, Choi BC, Jeong JH, Jang K, Lee HS, Yi SS (2013) Wide-band excited $Y_6(WMo)_{0.5}O_{12}$:Eu red phosphor for white light emitting diode: structure evolution, photoluminescence properties, and energy transfer mechanisms involved. Inorg Chem 52:11210–11217
56. Li H, Yang HK, Moon BK, Choi BC, Jeong JH, Jang K, Lee HS, Yi SS (2011) Crystal structure, electronic structure, and optical and photoluminescence properties of Eu(III) ion-doped $Lu_6Mo(W)O_{12}$. Inorg Chem 50:12522–12530
57. Chevire F, Clabau F, Larcher O, Orhan E, Tessier F, Marchand R (2009) Tunability of the optical properties in the $Y_6(W,Mo)(O,N)_{12}$ system. Solid State Sci 1:533–536

58. Yu RJ, Shin DS, Jang K, Guo Y, Noh HM, Moon BK, Choi BC, Jeong JH, Yi SS (2014) Photoluminescence properties of novel host-sensitized Y_6WO_{12}:Dy^{3+} phosphors. J Am Ceram Soc 97:2170–2176
59. Taupin AA (1973) Powder-diagram automatic-indexing routine. J Appl Crystallogr 6:380–−385
60. Evans IR, Howard JAK, Evans JSO (2005) The crystal structure of α-$La_2Mo_2O_9$ and the structural origin of the oxide ion migration pathway. Chem Mater 17:4074–4077
61. Alekseeva OA, Verin IA, Sorokina NI, Novikova NE, Kolesnikova DS, Voronkova VI (2010) Crystal structure of the metastable cubic βms phase of $La_2Mo_2O_9$ single crystal at T = 33 K. Kristallografiya 55:213–219; Crystallogr Rep 55:199−205
62. Shannon RD (1976) Revised effective ionic radii and systematic studies of interatomic distances in halides and chalcogenides. Acta Crystallogr Sect A Cryst Phys Diffr Theor Gen Crystallogr 32:751–767
63. Chun-Ju H, Xu Z, Chang-Song L, Xian-Ping W, Qian-Feng F (2008) Crystal structure of β-$La_2Mo_2O_9$ from first principles calculation. Chin Phys Lett 25:3342–3345
64. Fournier JP, Fournier J, Kohlmuller R (1970) Étude des systómes La_2O_3 – MoO_3, Y_2O_3 – MoO_3 et des phases Ln_6MoO_{12}. Bulletin de la Societe Chimique de France 12:4277
65. Aitken AE, Bartram SF, Juenke EF (1949) Crystal chemistry of the rhombohedral $MO_3{\cdot}3R_2O_3$ compounds. Inorg Chem 3(7):949
66. Bartram SF (1966) Crystal structure of the rhombohedral $MO_3{\cdot}3R_2O_3$ compounds (M = U, W, or MO) and their relation to ordered R_7O_{12} phases. Inorg Chem 5(5):749–754
67. Diot N, Benard-Rocherulle P, Marchand R (2000) X-ray powder diffraction data and rietveid refinement for Ln_6WO_{12}(Ln=Y, Ho). Powder Diffr 15(4):220
68. Yoshimura M, Ma J, Kakihana M (1998) Low-temperature synthesis of cubic and rhombohedral Y_6WO_{12} by a polymerized complex method. J Am Ceram Soc 81(10):2721–2724
69. Apostolov ZD, Sarin P, Haggerty RP, Kriven WM (2013) In-situ synchrotron X-ray diffraction study of the cubic to rhombohedral phase transformation in Ln_6WO_{12} (Ln = Y, Ho, Er, Yb). J Am Ceram Soc 96(3):987–994
70. Boulon G, Laversenne L, Goutaudier C, Guyot Y, Cohen-Adad MT (2003) Radiative and non-radiative energy transfers in Yb^{3+}-doped sesquioxide and garnet laser crystals from a combinatorial approach based on gradient concentration fibers. J Lumin 102/103:417–425
71. Canibano H, Boulon G, Palatella L, Guyot Y, Brenier A, Voda M, Balda R, Fernandez J (2003) Spectroscopic properties of new Yb^{3+}-doped $K_5Bi(MoO_4)_4$ crystals. J Lumin 102–103: 318–326
72. Legendziewicz J, Cybinska J, Guzik M, Boulon G, Meyer G (2008) Comparative study of crystal field analysis in Pr^{3+} and Yb^{3+}-doped K_2LaX_5 (X = Cl-, Br-) ternary halides and Yb^{3+}-doped $A_3Lu(PO_4)_2$ (A = Na^+, Rb^+) double phosphates. Charge transfer band observations of Yb^{3+}-doped systems. Opt Mater 30:1655–1666
73. Guzik M, Tomaszewicz E, Guyot Y, Legendziewicz J, Boulon G (2016) Spectroscopic properties, concentration quenching and Yb^{3+} site occupations in vacancied scheelite-type molybdates. J Lumin 169:755–764